| OF |
AD
A033185

END

DATE
FILMED

2-77
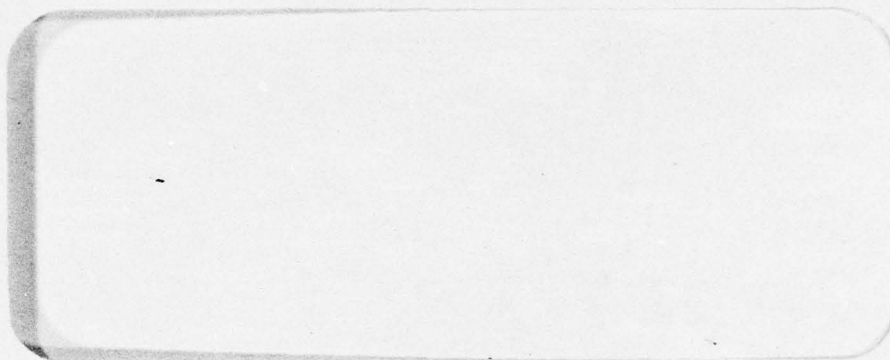
Bell Laboratories

FINAL REPORT.

OFFICE OF NAVAL RESEARCH

CONTRACT NUMBER NR 062-538

THE ORIGIN OF CUSPED WAVES
IN LAYERED FLUIDS.

by

Gary S. Deem

Bell Laboratories
Whippany, N. J.   07981

July 20, 1976

DDC

DEC 3 1976

RECEIVED

C

054550

THE ORIGIN OF CUSPED WAVES

IN LAYERED FLUIDS

Gary S. Deem

ABSTRACT

We establish conditions for the appearance of nonlinear "cusped waves" in density layered shear flows by means of computer simulations with a model set of initial mean density and shear velocity profiles. These waves occur when a region with gradient Richardson number $R_i > 1/4$ is initially confined between regions where $R_i < 1/4$. In other cases a closed-circulation, "cat's eye" pattern develops. Buoyancy forces dominate in the nonlinear evolution of cusped waves, whereas Reynolds shear stresses dominate in the development of cat's eyes. Cusped waves continue to extract energy from the mean shear approximately linearly in time, whereas cat's eyes have bounded energy content. Indirect evidence is presented for the existence of cusped wave instabilities in the ocean.

1. Introduction

Extensive horizontal layers are a persistent feature of stably stratified flows. These have been observed in vertical profiles of temperature and salinity in the oceans (e.g., Elliott, et al., 1974) and in the temperature structure of the atmospheric boundary layer during night-time radiation inversion (Turner, 1973). Photographs by divers in the seasonal thermocline of the Mediterranean (Woods, 1968) have shown that a long wavelength internal wave propagating on a thin interfacial "sheet" between different constant temperature and density layers can lead to shear instabilities of the Kelvin-Helmholtz type. Examples of shear-induced instabilities have also been observed in the atmosphere with radar sounders (Gossard and Hooke, 1975). Similar examples of this instability have been studied in the laboratory by Thorpe (1973), using a density layered fluid tube.

The nonlinear development of shear - induced instabilities in the oceans provides a mechanism for enhanced vertical transport of heat and momentum. Shear instabilities may therefore be an important component in thermocline formation (Munk, 1972). Woods and Wiley (1972) have suggested that many of the observed details of thermocline temperature structure can be attributed to shear instabilities caused by long internal waves propagating on sheets.

According to these authors, the turbulent billows which form entrain fluid from either side of the interfacial region until the sheet thickness grows to several times its original value. Internal wave shear eventually causes neighboring billows to overlap, providing a possible mechanism for replacement of the original interface by two sheets. Subsequent internal waves lead to further splitting, resulting in vertical transport. Garrett and Munk (1972) have used these ideas to estimate the depth dependence of vertical and horizontal diffusivities in the ocean.

The experiments of Thorpe (1973) indicate that the sheet-splitting mechanism of Woods and Wiley requires further investigation. The vertically spreading turbulent regions observed by Thorpe show no evidence for large gradients in density or horizontal velocity at their edges. These experiments also disagree with a qualitative description of sheet spreading advanced by Businger (1969). The latter argues that spreading ceases when the mean gradient Richardson number of the turbulent region rises to unity. Thorpe, however, measures fully developed mean gradient Richardson numbers closer to 0.3.

The present paper discusses the results of extensive two-dimensional numerical simulations which address the above issues. The fully developed states which result from shear instabilities on thermal sheets in the ocean possess several features which make them attractive for numerical

simulation. They are first of all characterized by moderate Reynolds numbers R_e (based on sheet thickness and mean shear velocity) of order 1000 (Thorpe, 1973), corresponding to microscale Reynolds numbers of order 100. In contrast to most other interesting turbulent geophysical flows, numerical simulations with Reynolds numbers of this order are possible without introducing phenomenological treatments of Reynolds stress terms (Fox and Lilly, 1972; Case, et al., 1973). Buoyancy forces also act to suppress vertical turbulent motions and to couple energy into large-scale internal waves. Finally, the initial shear instability and many features of the fully developed billows are two-dimensional effects.

Calculations are presented for Prandtl numbers $P_r = 10$, relevant to thermal layers in the ocean, and for Reynolds numbers $R_e \leq 200$, slightly lower than typical billow mixing events in the ocean and in Thorpe's experiments. However, results obtained at these Reynolds numbers are sufficiently similar to observed phenomena to be of considerable interest. In particular, the origin of "cusped waves" is explained. These waves have been observed in a variety of turbulent mixing experiments (Ellison and Turner, 1959; Lofquist, 1960; Thorpe, 1968; Moore and Long, 1971) and in the atmosphere (Gossard and Hooke, 1975). Thorpe (1973) states that these waves appear at about the time of the onset of turbulence. They first appear (or break) in the upper layer of fluid, but at later times they are

observed moving in opposite directions on either side of the interface.

The results of the present paper confirm a conjecture by Thorpe (1973) that cusped waves are the finite amplitude result of shear instabilities associated with small gradient Richardson numbers at the sheet edges and large Richardson numbers $\geq 1/4$ within the sheet. Calculations show that this instability is asymmetric and first appears in the upper portion of the flow. In other cases, where the Richardson number is less than 1/4 within the sheet, the instability is symmetric and develops into a familiar "cat's eye" circulation pattern. The latter situation has been studied numerically by Patnaik, et al. (1976), for $P_r < 1$.

Our calculations also reveal that buoyancy forces dominate Reynolds stresses in the evolution of cusped waves, so that these are a truly buoyant phenomenon. The reverse is true in the development of the cat's eye circulation pattern, which is a basically nonbuoyant phenomenon. Moreover, cusped waves continue to extract energy from the mean shear and to increase the sheet thickness at very long times; the cat's eye pattern grows to a maximum vertical extent and energy content and then slowly decays by viscosity.

The possible importance of the cusped wave instability in the ocean is examined in a concluding section. Using a model thermocline, similar to that reported by Woods (1968) in the summer thermocline near Malta, it is

shown that the velocity and thermal structure of an internal wave modified by the presence of a thermal sheet is, in many cases, more favorable to the formation of cusped waves than cat's eyes.

2. Linear Stability

We first present relevant properties of shear induced instabilities due to a thin horizontal sheet of enhanced thermal gradient. We consider unperturbed horizontal velocity and density profiles

$$\bar{u}(z) = U_0 \text{erf}\left(\frac{1}{2}\sqrt{\pi}\ z/\delta\right), \tag{2.1}$$

$$\bar{\rho}(z) = \rho_0 \exp\left[-\beta/R\ \text{erf}\left(\frac{1}{2}\sqrt{\pi}\ Rz/\delta\right)\right], \tag{2.2}$$

where z $(-\infty < z < \infty)$ is the vertical coordinate, U_0/δ and ρ_0 are the horizontal shear and density at the sheet center $z = 0$, R is the ratio of half-widths of the velocity and density profiles, and $\beta = R \sinh^{-1}\left(\frac{1}{2}\ \Delta\rho/\rho_0\right)$. Here $\Delta\rho$, the total density difference across the sheet, is related to the thermal difference ΔT. For example, in water near 20°C, small density and thermal variations are related by

$$\frac{\Delta\rho}{\rho_0} = -0.057\ \frac{\Delta T}{T_0}, \tag{2.3}$$

where the mean temperature T_0 is expressed in degrees Kelvin. Hazel (1972) has studied similar (hyperbolic tangent) profiles for various thickness ratios R.

In the following, we make quantities nondimensional with appropriate combinations of δ, U_0 and ρ_0. The local gradient Richardson number corresponding to (2.1) and (2.2) becomes

$$R_1(z) = J \exp\left| - \frac{\pi}{4} (R^2-2)z^2 \right|, \qquad (2.4)$$

where

$$J = \beta g \delta / U_0^2$$

is the <u>overall</u> Richardson number based on the sheet thickness δ. For $R < \sqrt{2}$, the gradient Richardson number has a minimum at the sheet center and profiles (2.1) and (2.2) are stable for $J \geq \frac{1}{4}$. Figure 1 shows neutral stability curves which we have computed from the inviscid Taylor-Goldstein equation in the Boussinesq approximation

$$(\bar{u}-c) \left(\frac{d^2}{dz^2} - \alpha^2 \right) \phi - \left(\frac{d^2\bar{u}}{dz^2} - \frac{N^2}{\bar{u}-c} \right) \phi = 0. \qquad (2.5)$$

Here $\phi(z)$ is the vertical profile of the perturbation stream function

$$\psi'(x,z,t) = \text{Re}\left\{ \phi(z) \exp[i\alpha(x-ct)] \right\} \qquad (2.6)$$

and α and $c = c_r + ic_i$ are a dimensionless wave number and complex phase speed. $N(z)$ is a dimensionless mean Brunt-Väisälä frequency

$$N^2(z) = - F_r^{-1} \frac{d}{dz} \ln \bar{\rho} , \qquad (2.7)$$

where $F_r = U_0^2/g\delta$ is a Froude number.

The growth rates αc_i of the most unstable disturbances are shown (dashed line) for $R = 1$ in the upper half of Figure 1. The lower part of the figure shows neutral stability curves (where $c = 0$) as a function of R. For $\alpha < \sqrt{2}$ the neutral stability curves bound the region of instability in the $\alpha - J$ plane.

For $R > \sqrt{2}$ (shear profile wider than density profile) the gradient Richardson number approaches zero for large $|z|$. Figure 2 shows stability boundaries for $R = 3.5$. The neutral stability curve bounds the region of stability for one mode, but another mode is always unstable (Hazel, 1972). Inside of the solid curve the instability is a standing wave ($c_r = 0$) and outside it is progressive. The figure also shows that the locus of the most unstable mode moves to shorter wavelengths as J is increased above $1/4$.

Figure 3 shows real and imaginary parts of the complex stream eigenfunction $\phi(z)$ normalized so that $\phi(0) = 1$. The most unstable $\phi(z)$ is shown for various R and J. Case (b) is typical for $R < \sqrt{2}$ and does not differ significantly from the $J = 0$ unstratified case (a). For case (c), the entire flow satisfies $R_i < \frac{1}{4}$ and the eigenfunctions are relatively broad. Case (d) is a propagating mode ($c_r = 0.330$) with $R = 3.5$ and $J = 0.4$. The most unstable perturbation is asymmetric about $z = 0$. As we shall see, this asymmetry leads to nonlinear cusped waves in the upper half of the shear region.

3. Numerical Scheme

3.1 Boussinesq Equations

We assume that local density variations are small with respect to ρ_0 and are linearly related to thermal variations, as in (2.3). We shall consider the nonlinear, two-dimensional, late time evolution of small perturbations of profiles (2.1) and (2.2) according to the Boussinesq equations

$$\partial_t \underline{u} + \nabla \cdot (\underline{u} \circ \underline{u}) = -\nabla p - F_r^{-1} \rho \underline{\hat{z}} + R_e^{-1} \nabla^2 \underline{u}, \tag{3.1}$$

$$\partial_t \rho + \nabla \cdot (\rho \underline{u}) = P_e^{-1} \nabla^2 \rho, \tag{3.2}$$

$$\nabla \cdot \underline{u} = 0. \tag{3.3}$$

Here $\circ$ denotes a dyadic tensor product,

$$\nabla = (\partial_x, \partial_z), \tag{3.4}$$

$$\underline{u}(\underline{x}, t) = [u(x,z,t), w(x,z,t)] \tag{3.5}$$

is the two-dimensional velocity in a vertical $x - z$ plane, p is the nondimensional pressure, $\underline{\hat{z}}$ is the unit normal in the vertical direction, R_e is the Reynolds number

$$R_e = \frac{U_0 \delta}{\nu}, \tag{3.6}$$

ν is the kinematic viscosity, P_e is the Peclet number

$$P_e = R_e P_r, \tag{3.7}$$

P_r is the Prandtl number

$$P_r = \nu/\kappa$$

and κ is the thermal diffusion coefficient. In the following we use values $P_r = 10$ and $F_r = 0.001$, representative of the ocean (Woods, 1968).

3.2 Boundary Conditions

We use periodic boundary conditions for $0 \leq x \leq 2\pi/\alpha$ in the horizontal direction. We confine the flow between horizontal planes $-\frac{D}{2} \leq z \leq \frac{D}{2}$ in the vertical direction and impose finite boundary conditions

$$\partial_z u = 0, \; w = 0, \; \rho = \rho_+ \text{ or } \rho_- \quad (z = \pm \tfrac{1}{2} D), \qquad (3.9)$$

where ρ_+ and ρ_- are constant density values at the upper and lower boundaries, as determined by (2.2). Conditions (3.9) guarantee that vorticity

$$\omega = -\partial_z u + \partial_x w \qquad (3.10)$$

is not produced at the upper and lower boundaries. The pressure boundary condition corresponding to (3.9) follows from (3.1) as

$$\partial_z p = -F_r^{-1}\rho = \text{constant} \quad \left(z = \pm \tfrac{1}{2} D\right). \qquad (3.11)$$

3.3 Spatial Discretization

We use a numerical scheme similar to that described by Zabusky and Deem (1971). Accordingly, discretized,

staggered velocities and densities $u_{m+\frac{1}{2},n}$, $w_{m,m+\frac{1}{2}}$ and $\rho_{m,n+\frac{1}{2}}$ are defined on lattice cell sides and pressures $p_{m,n}$ are defined at cell centers for $m = 1, \ldots, M$ and $n = 1, \ldots, N$. Equations (3.1) and (3.3) are replaced by

$$\partial_t w_{m,n+\frac{1}{2}} + \delta_x\left(u_{m-\frac{1}{2},n+\frac{1}{2}} w_{m-\frac{1}{2},n+\frac{1}{2}}\right) + \delta_z\left(w^2_{m,n}\right)$$

$$= -\delta_z p_{m,n} - F_r^{-1} \rho_{m,n+\frac{1}{2}} + R_e^{-1}\left[\delta_x\left(\delta_x w_{m-1,n+\frac{1}{2}}\right) + \delta_z\left(\delta_z w_{m,n-\frac{1}{2}}\right)\right],$$

$$(3.12)$$

$$\delta_x u_{m-\frac{1}{2},n} + \delta_z w_{m,n-\frac{1}{2}} = 0, \qquad (3.13)$$

with similar equations for $u_{m+\frac{1}{2},n}$ and $\rho_{m,n+\frac{1}{2}}$. Here δ_x and δ_z are one-sided, forward difference operators in the x and z directions, respectively. Quantities such as $w_{m,n}$ are appropriately centered linear averages

$$w_{m,n} = \frac{1}{2}\left(w_{m,n-\frac{1}{2}} + w_{m,n+\frac{1}{2}}\right), \qquad (3.14)$$

etc. In the absence of density variations, the above spatial discretization guarantees conservation of momentum and energy (for $\nu = 0$).

3.4 Temporal Discretization

We use a split-step approach to advance in time. Auxiliary velocities $u^*_{m+\frac{1}{2},n}$ and $w^*_{m,n+\frac{1}{2}}$ are first computed using a time-centered, three time-level "leapfrog" scheme, which omits the pressure and viscosity terms. Time-centered pressures are then computed from the Poisson equation

$$\delta_x\left(\delta_x p_{m-1,n}\right) + \delta_z\left(\delta_z p_{m,n-1}\right) = \frac{1}{2\Delta t}\left(\delta_x u^*_{m-\frac{1}{2},n} + \delta_z w^*_{m,n-\frac{1}{2}}\right),$$

$$(3.15)$$

with horizontal boundary condition (3.11), where Δt is the time step. Equation (3.15) is solved exactly and noniteratively using cyclic reduction methods (Buneman, 1969; Schumann and Sweet, 1976). New auxiliary velocities are then computed from

$$u^{**}_{m+\frac{1}{2},n} = u^*_{m+\frac{1}{2},n} - 2\Delta t\, \delta_x p_{m,n}. \qquad (3.16)$$

Final velocities at the new time $t + \Delta t$ are given by

$$u_{m+\frac{1}{2},n} = u^{**}_{m+\frac{1}{2},n} + \frac{2\Delta t}{R_e}\left[\delta_x\left(\delta_x u^{**}_{m-\frac{1}{2},n}\right) + \delta_z\left(\delta_z u^{**}_{m+\frac{1}{2},n-1}\right)\right],$$

$$(3.17)$$

with a similar expression for $w_{m,n+\frac{1}{2}}$. The density $\rho_{m,n+\frac{1}{2}}$ is advanced in a similar manner, using velocities $u_{m+\frac{1}{2},n}$ and $w_{m,n+\frac{1}{2}}$ at the centered time t.

For large Reynolds numbers, the above scheme is second-order accurate $O(\Delta x^2 + \Delta z^2 + \Delta t^2)$. In our calculations, this scheme remains stable for $\Delta t \leq \min(\Delta x/u, \Delta z/w)$, where Δx and Δz are the constant x and z lattice spacings. Moreover, it retains the inviscid time reversibility of the Navier-Stokes equations and guarantees incompressibility (3.13) to within roundoff error of the computer.

For lower accuracy computers it is preferable to eliminate the large static pressure by replacing ρ and p in (3.1) with the perturbed density and pressure

$$\tilde{\rho} = \rho - \frac{\rho_+ + \rho_-}{2} - \frac{\rho_+ - \rho_-}{D} z, \qquad (3.18)$$

$$\tilde{p} = p + F_r^{-1} \left[\frac{\rho_+ + \rho_-}{2} z + \frac{\rho_+ - \rho_-}{2D} z^2 \right]. \qquad (3.19)$$

The perturbed pressure then satisfies (3.15) with Neumann boundary conditions

$$\partial_z \tilde{p} = 0 \quad \left(z = \pm \frac{1}{2} D \right). \qquad (3.20)$$

3.5 Initial Conditions

We consider only the growth of a single perturbing mode, using initial mean profiles (2.1), (2.2) and the complex eigenfunctions ϕ of Figure 3 (altered slightly to make them vanish at the boundaries $z = \pm \frac{1}{2} D$). From (2.6) and the perturbed density equation, we have

$$u(x,z,0) = \overline{u}(z) + \eta\partial_z R_e\left\{\phi(z)\exp(i\alpha x)\right\}, \qquad (3.21)$$

$$v(x,z,0) = -\eta\partial_x R_e\left\{\phi(z)\exp(i\alpha x)\right\}, \qquad (3.22)$$

$$\rho(x,z,0) = \overline{\rho}(z) + \eta R_e\left\{\frac{\phi(z)\partial_z\overline{\rho}(z)}{\overline{u}(z) - c}\exp(i\alpha x)\right\}. \qquad (3.23)$$

Here c is the complex linear phase speed and η is a small parameter (0.1 or less in our computations).

We have not studied nonlinear interaction between modes (Zabusky and Deem, 1971) or subharmonic generation (Patnaik, et al., 1976) in the present paper, although these subjects are of considerable importance in observed two dimensional shear flows (Winant and Browand, 1973).

In succeeding sections, we consider separately cases where $R < \sqrt{2}$ and $R > \sqrt{2}$, where R is the relative velocity shear thickness in (2.2). Table 1 summarizes the physical and numerical parameter ranges which we have studied.

4. Nonlinear Dynamics for R = 1

Figures 4 and 5 show the nonlinear development of the fastest growing mode $\alpha = 0.43$ for R = 1 and J = 0.1. Figure 4 gives constant density contours and Figure 5 gives constant vorticity contours (solid) and streamlines (dotted). The flow develops into a cat's eye pattern, characterized by closed streamlines at the center of the flow, where a significant portion of fluid becomes confined. After t = 40

the pattern is fully developed and begins to decay due to viscosity and thermal diffusivity. The results are not significantly altered if we increase D = 10 (Run 1) to D = 16 (Run 2).

Figure 6 shows vertical profiles for the horizontally averaged velocity $\bar{u}(z)$, density $\bar{\sigma}(z) = 1000 \cdot [\bar{\rho}(z)-1]$ (Phillips, 1969) and gradient Richardson number $\bar{R}_i(z)$ at a late time t = 150 (Run 2). Corresponding curves at t = 0 are indicated with dashed lines. We note that $\bar{R}_i(z)$ approaches zero in the outer flow near $|z| = 5$ and has an average value of approximately 0.29 in the intervening flow region.

Figure 7 shows the time dependent behavior of the momentum and density vertical thicknesses, normalized with their values at t = 0. Here Δ_u and Δ_ρ are defined, respectively, as the vertical distances between z values where $\bar{u}$ and $\bar{\rho}$ come to within 90% of their values at the upper and lower edges of the flow. In the present case, where $R < \sqrt{2}$, the density profile spreads by less than a factor of two, whereas the momentum profile continues to grow slowly, presumably as the result of viscosity. The oscillations evident in the figure are the result of a time periodic nutation of the central elliptical streamline pattern in Figure 5 (Zabusky and Deem, 1971; Patnaik, et al., 1976).

Figure 8 shows time evolution of the fluctuation kinetic energy

$$E_f = \frac{1}{2} \langle u'^2 + w'^2 \rangle , \qquad (4.1)$$

the Reynolds shear stress

$$S = - \langle \overline{u'w'} \cdot \partial_z \overline{u} \rangle , \qquad (4.2)$$

the buoyancy flux

$$N = - F_r^{-1} \langle \rho'w' \rangle , \qquad (4.3)$$

and the dissipation rate

$$\epsilon = R_e^{-1} \langle (\partial_x u')^2 + (\partial_z u')^2 + (\partial_x w')^2 + (\partial_z w')^2 \rangle \quad (4.4)$$

for Run 2. Here, we divide the flow variables into their down-
stream averaged mean and fluctuating parts (e.g., $u = \overline{u} + u'$)
and we use braces to denote averages over the entire flow.
The above quantities satisfy the fluctuation kinetic energy
equation (Phillips, 1969)

$$\frac{d}{dt} E_f = S + N - \epsilon . \qquad (4.5)$$

so that S, N and ϵ are a measure of the overall contributions
of shear, buoyancy and viscous dissipation in the balance
of kinetic energy. In all of our calculations the Reynolds
number is sufficiently large so that ϵ is of secondary
importance (Figure 8).

Figure 8 shows a characteristic feature of the
cat's eye pattern, namely that shear stress is generally
larger than buoyancy flux.

5. Nonlinear Dynamics for R = 3.5

For $R > \sqrt{2}$ the initial gradient Richardson number falls to zero for large $|z|$ and has a maximum J at z = 0. We consider cases where J < 1/4 and J > 1/4 in this section.

Figures 9 and 10 show density, vorticity and stream function contours for the nonlinear development of the fastest growing mode α = 0.38 with R = 3.5 and J = 0.1 (Run 3). Figure 11 shows the time behavior of E_f, S, N and ϵ (Run 4). As one would expect, the instability is more energetic than for $R < \sqrt{2}$ (Figure 8), but the final state is similar to the shear stress dominated cat's eye pattern of the previous section.

Figures 12 and 13 show that <u>cusped</u> <u>waves</u> result for R = 3.5 and J = 0.4. The Reynolds number is R_e = 100 (Run 7). The instability is nonsymmetric and propagating and develops preferentially into the lighter fluid above the central shear layer.

Figure 14 shows the same flow at very long times. The density contours reveal a secondary wave (arrows) which moves to the left in a direction opposite to and with a speed equal to that of the primary cusped wave. Examination of the central stream function contours at t = 160 and t = 200 shows that when the two waves are in close proximity, a closed circulation region forms.

Figure 15 shows that at higher Reynolds numbers (R_e = 200, Run 9) the cusped wave breaks.

The flow is again characterized by a pair of nonlinear waves moving in opposite directions. At late times the outer portions of the lower, secondary wave also show evidence of breaking.

We have performed calculations at higher Reynolds numbers (Table 1), but the present numerical resolution is not sufficient to resolve all the fine scale features which develop. However, we do call attention to a trend whereby the upper and lower vortex regions become symmetric at late times.

Figure 16 shows the time behavior of E_f, S, N and ϵ for Runs 7 and 9. We see that the formation of cusped waves is a buoyancy dominated phenomenon very different from the cat's eye case. Moreover, cusped waves continue to extract energy from the mean flow and E_f grows linearly, on the average.

Figure 16 shows that breaking of cusped waves (upper dashed curve for $R_e = 200$) is a more energetic process than when the waves do not break. This is consistent with an earlier observation that cusped waves are buoyancy dominated, so that they depend strongly on the distribution of density.

Figure 17 shows the time dependences of the density and momentum thicknesses for $R = 3.5$ in the cases $J = 0.4$ and $J = 0.1$ (Runs 7 and 4). The density thickness for the cusped wave case (a) grows linearly even at very long times.

Figure 18 shows the z dependences of $\bar{\sigma}$, $\bar{u}$ and $\bar{R}_1$ with $R = 3.5$, and $J = 0.4$ and 0.1 at a time $t = 130$, compared with their initial values (dashed lines). The strongly

unstable cat's eye case (a, d and f) shows evidence for sheet splitting, characterized by a nearly constant central density region bounded by regions of large Richardson number.

At the time shown in Figure 18, the average Richardson number over the central flow region (where $\overline{R}_1(z) \neq 0$) is 0.29 for the cat's eye case (f) and 0.27 for the cusped wave case (e). This, together with a similar observation in Section 4, is in agreement with the experimental results of Thorpe (1973), who observes average gradient Richardson numbers of order 0.3 in the fully developed central flow region resulting from two dimensional shear induced instabilities. These results do not support heuristic arguments by Businger (1969) that the average gradient Richardson number should approach unity at late times.

6. Conditions for Cusped Wave Instability in the Malta Thermocline

The significance of cusped wave instabilities in the ocean is not understood. Since this instability predicts a slow but persistent linear spreading of the interfacial region, it is of interest to explore conditions for the appearance of cusped waves in the thermocline. In this section we examine how long wavelength internal waves are modified by the presence of a thin sheet of enhanced thermal gradient. We will be interested in conditions where an appropriately defined local shear thickness exceeds the

sheet thickness by, say, $\sqrt{2}$. It is useful to employ dimensional quantities in this discussion.

We model the mean thermocline thermal gradient with a Gaussian profile, as shown in Figure 19. Here N^2, the dimensional mean Brunt-Väisälä frequency in the absence of sheets, is plotted versus depth in meters. The mean Malta profile (Woods, 1968) is shown for comparison. We assume that a single sheet is located at the thermocline center, taken as $z = 0$ in the following, and that the total N^2 is given by

$$N^2(z) = N_0^2 \exp\left[-\frac{1}{2}\left(\frac{z}{H}\right)^2\right] + N_m^2 \exp\left[-\frac{1}{2}\left(\frac{z}{h}\right)^2\right],$$

(6.1)

where $N_m^2 \gg N_0^2$ and $h \ll H$. Values typical of those in the Malta thermocline are $H = 550$ cm, $h = 5$ cm, $N_0^2 = 0.0008$ sec^{-2} and $N_m^2 = 0.004$ sec^{-2}, corresponding to total temperature differences of $6.3°$C and $0.26°$C across the thermocline and sheet, respectively.

There are an infinite number of internal wave modes of given wavelength L having different real wave velocities c. We have extensively studied properties of the lowest shear mode (whose maximum shear occurs at $z = 0$) as a function of L/h, H/h and $\tilde{N}_0^2$. This involves solution of the eigenvalue equation for internal waves in the Boussinesq approximation (Phillips, 1969, pg. 161) with boundaries at $z = \pm \infty$ (no surface waves). The results are summarized in

the wave stability diagrams of Figures 20 and 21. Here,
we eliminate the unknown velocity U_0 in the overall
Richardson number J in favor of the internal wave amplitude
a and define a modified Richardson number

$$\tilde{J} = \left(\frac{a}{h}\right)^2 J. \qquad (6.2)$$

We also define, somewhat arbitrarily, a <u>local</u> shear thickness
ratio R, equal to the value of $\sqrt{2}z/h$ where the computed
horizontal wave velocity rises to 0.52 of its maximum value
(this reduces to the previous meaning for R in Section 2
for horizontal wave velocities and sheet density of the
form (2.1) and (2.2), where $\delta = \sqrt{\pi/2}$ Rh). For small $\tilde{N}_0^2$,
corresponding to large thermal steps, Figure 20 shows that the
internal waves are substantially altered near the sheet and
R is of order unity or less except for very long wavelengths
(hatched region to the right). For somewhat larger $\tilde{N}_0^2$
(smaller thermal steps) the sheet is less effective in
altering the local shear thickness, and interesting parameter
regions occur where R is substantially greater than unity
(Figure 21), where we expect cusped wave instability.

The $\tilde{J}$ contours in Figures 20 and 21 indicate
that shear instability leading to cat's eyes ($J < 1/4$) occurs
only for relatively large amplitude internal waves. For
example with $\tilde{N}_0^2 = 0.2$ (Figure 20), H/h = 110 and L/h = 150,
it is necessary that a/L = 0.16 to reduce J to 1/4. Amplitude-
wavelength ratios of this order are approaching values where

nonlinear breaking occurs. This point is further illustrated in Figure 21 for the case of a weak thermal step. The heavy solid curve represents the locus of points where $J = 1/4$ and, simultaneously, the mean-square wave slope is unity. Above this curve, nonlinear breaking is more likely than the cat's eye shear instability.

The results in this section are heuristic in the sense that we have not studied the detailed stability characteristics of internal wave profiles modified by the presence of sheets. This would be a considerably more ambitious undertaking which is complicated by the periodic time variation of the actual internal wave shear. The results suggest, however, that cusped wave instability may be a commonly occurring mechanism which gives sheet spreading (i.e., vertical heat transport) by relatively small amplitude internal waves with $J > 1/4$.

7. Conclusion

We have established conditions which lead to nonlinear cusped waves in layered, shear flows. For the model error function mean velocity and density profiles used, we find that cusped wave instability occurs when the length scale of the shear layer exceeds that of the density transition layer by $\sqrt{2}$ and, simultaneously, the centerline Richardson number exceeds $1/4$. In other cases instability develops into a familiar cat's eye pattern. The cusped wave instability is of special interest in that it continues to extract energy

from the mean shear, whereas the cat's eye pattern is bounded in its energy content and vertical extent. We have presented indirect evidence that conditions for the cusped wave instability may be relatively common for realistic thermoclines, sheet thicknesses and internal wave amplitudes.

8. Acknowledgments

Run	M,N	D	α	R	J	η	R_e	P_r	Δt	t_{max}
1	64,129	10	0.43	1	0.1	0.05	100	10	0.1	80
2	64,129	16	0.43	1	0.1	0.05	100	10	0.1	150
3	64,129	10	0.38	3.5	0.1	0.05	100	10	0.05	80
4	64,129	16	0.38	3.5	0.1	0.05	100	10	0.1	150
5	41,129	14	0.50	3.5	0.4	0.1	1000	10	0.05	100
6	64,129	10	0.50	3.5	0.4	0.02	1000	1	0.1	200
7	64,129	10	0.50	3.5	0.4	0.05	100	10	0.1	200
8	64,129	10	0.50	3.5	0.4	0.02	100	10	0.05	100
9	64,129	10	0.50	3.5	0.4	0.02	200	10	0.05	100
10	64,129	10	0.50	3.5	0.4	0.02	100	10	0.1	100
11	64,129	16	0.50	3.5	0.4	0.02	100	20	0.1	100
12	64,129	10	0.50	3.5	0.4	0.02	200	4	0.1	100

Table 1. Physical and Computational Parameters

REFERENCES

Buneman, O., "A Compact Non-Iterative Poisson Solver,"
Rep. SU-IPR-294, Institute for Plasma Research, Stanford
University, 1969.

Businger, J. A., "On the Energy of Clear Air Turbulence,"
in Clear Air Turbulence and its Detection (ed., Y. H. Pao
and A. Goldberg), Plenum Press, 1969.

Case, K. M., Dyson, F. J., Friedman, E. A., Grosch, C. E.,
Perkins, F. W., "Numerical Simulation of Turbulence,"
SRI Tech, Rept. JSR-73-3, November, 1973.

Elliott, A. J., Howe, M. R., and Tait, R. I., "The Lateral
Coherence of a System of Thermo-Haline Layers in the Deep
Ocean," Deep-Sea Res. 21, 95 (1974).

Ellison, T. H. and Turner, J. S., "Turbulent Entrainment
in Stratified Flows," J. Fluid Mech. 6, 423 (1959).

Fox, D. G. And Lilly, D. K., "Numerical Simulation of
Turbulent Flows," Rev. of Geophys. and Sp. Physics 10,
51 (1972).

Garrett, C. and Munk, W., "Oceanic Mixing by Breaking
Internal Waves," Deep-Sea Res. 19, 823 (1972).

Gossard, E. E. and Hooke, W. H., Waves in the Atmosphere,
Elsevier Scientific Pub. Co., 1975.

Hazel, P., "Numerical Studies of the Stability of Inviscid
Stratified Shear Flows," J. Fluid Mech. 51, 39 (1972).

Lofquist, K., "Flow and Stress Near an Interface Between
Stratified Fluids," Phys. Fluids 3, 158 (1960).

Moore, M. J. and Long, R. R., "An Experimental Investigation
of Turbulent Stratified Shearing Flow," J. Fluid Mech. 49,
635 (1971).

Munk, W. H., "Turbulence in a Stratified Ocean," in
Statistical Models and Turbulence (ed., J. Ehlers, et al.),
Springer-Verlag, 1972.

Patnaik, P. C., Sherman, F. S., and Corcos, G. M., "A
Numerical Simulation of Kelvin-Helmholtz Waves of Finite
Amplitude," J. Fluid Mech. 73, 215 (1976).

Phillips, P. M., The Dynamics of the Upper Ocean, Cambridge University Press, 1969.

Schumann, U. and Sweet, R. A., "A Direct Method for the Solution of Poisson's Equation with Neumann Boundary Conditions on a Staggered Grid of Arbitrary Size," J. Comp. Phys. 20, 171 (1976).

Thorpe, S. A., "A Method of Producing a Shear Flow in a Stratified Fluid," J. Fluid Mech. 32, 693 (1968).

Thorpe, S. A., "Experiments on the Stability of Stratified Shear Flows," Radio Science 4, 1327 (1969).

Thorpe, S. A., "Turbulence in Stably Stratified Fluids," Boundary Layer Meteorol. 5, 95 (1973).

Thorpe, S. A., Experiments on Instability and Turbulence in a Stratified Shear Flow," J. Fluid Mech. 61, 731 (1973).

Turner, J. S., Buoyancy Effects in Fluids, Cambridge University Press, 1973.

Winant, C. D. and Browand, F. K., "Vortex Pairing: the Mechanism of Turbulent Mixing-Layer Growth at Moderate Reynolds Number," J. Fluid Mech. 63, 237 (1974).

Woods, J. D., "Wave-Induced Shear Instability in the Summer Thermocline," J. Fluid Mech. 32, 791 (1968).

Woods, J. D., "CAT Under Water," Weather 23, 224 (1968).

Woods, J. D. and Wiley, R. L., "Billow Turbulence and Ocean Microstructure," Deep-Sea Res. 19, 87 (1972).

Zabusky, N. J. and Deem, G. S., "Dynamical Evolution of Two-Dimensional Unstable Shear Flows," J. Fluid Mech. 47, 353 (1971).

FIGURE CAPTIONS

Figure 1. Stability Boundary for R = 1 and Neutral Stability Curves for Various R (Error Function Profiles).

Figure 2. Stability Boundaries for R = 3.5 (Error Function Profiles).

Figure 3. Vertical z Dependencies of the Real and Imaginary Parts of the Most Rapidly Growing Eigen Functions for Various R and J.

Figure 4. Constant Density Contours to t = 80. R = 1, J = 0.1, α = 0.43, R_e = 100, P_r = 10 (Run 1).

Figure 5. Constant Vorticity Contours (Solid) and Streamlines (Dotted) Corresponding to Figure 4.

Figure 6. Vertical Profiles of the Mean Density Perturbation $\bar{\sigma}$ = 1000·($\bar{\rho}$-1), Mean Velocity $\bar{u}$ and Mean Richardson Number $\bar{R}_i$ at Times t = 0 (Dashed) and 150. R = 1, J = 0.1, α = 0.43, R_e = 100, P_r = 10 (Run 2).

Figure 7. Momentum and Density Thicknesses Δ_u and Δ_ρ (Normalized by their Initial Values) Versus Time. Conditions of Figure 6.

Figure 8. Fluctuation Energy, Reynolds Shear Stress, Buoyancy Flux and Dissipation Rate Versus Time. Conditions of Figure 6.

Figure 9. Density Contours to t = 80. R = 3.5, J = 0.1, α = 0.38, R_e = 100, P_r = 10 (Run 3).

Figure 10. Vorticity Contours (Solid) and Streamlines (Dotted) Corresponding to Figure 9.

Figure 11. Fluctuation Energy, Reynolds Shear Stress, Buoyancy Flux and Dissipation Rate Versus Time. R = 3.5, J = 0.1, α = 0.38, R_e = 100, P_r = 10 (Run 4).

Figure 12. Cusped Wave Constant Density Contours for R = 3.5, J = 0.4, α = 0.5, R_e = 100, P_r = 10 (Run 7).

Figure 13. Vorticity Contours and Streamlines Corresponding to Figure 12.

Figure 14. Long Time Behavior Corresponding to Figures 12 and 13. The Arrows Indicate the Position of a Secondary Wave Moving to the Left.

Figure 15. Breaking of Cusped Wave Density Contours for $R = 3.5$, $J = 0.4$, $\alpha = 0.5$, $R_e = 200$, $P_r = 10$ (Run 9).

Figure 16. Fluctuation Energy, Reynolds Shear Stress, Buoyancy Flux and Dissipation Versus Time. $R = 3.5$, $J = 0.4$, $\alpha = 0.5$, $P_r = 10$, $R_e = 100$ (Run 7). The Upper Dashed Curve Shows E_f at $R_e = 200$ (Run 9) for a Breaking Cusped Wave.

Figure 17. Density and Momentum Thicknesses Versus Time for $R = 3.5$ and $P_r = 10$. (a) and (c) Give Cusped Wave Formation with $J = 0.4$ (Run 7). (b) and (d) Give Cat's Eye Formation with $J = 0.1$ (Run 4).

Figure 18. Vertical Profiles of the Mean Density Perturbation and Mean Velocity at Times $t = 0$ (Dashed) and 130. Conditions of Figure 17.

Figure 19. Mean Thermocline Model. The Square Brunt-Väisälä Frequency (sec^{-2}) is shown Versus Depth (meters).

Figure 20. Lowest Shearing Mode Internal Wave Stability Diagram for $\tilde{N}_o^2 = 0.2$. Constant R (---) and $\tilde{J}$(—) Contours. The Lowest Shearing Mode Does Not Exist in the Left Hatched Region. The Circle Corresponds Approximately to Conditions Reported by Woods and Wiley (1972) for Malta.

Figure 21. Internal Wave Stability Diagram for $\tilde{N}_0^2 = 0.4$. Constant R (---) and $\tilde{J}$ (—) Contours. The heavy solid line is discussed in the text.
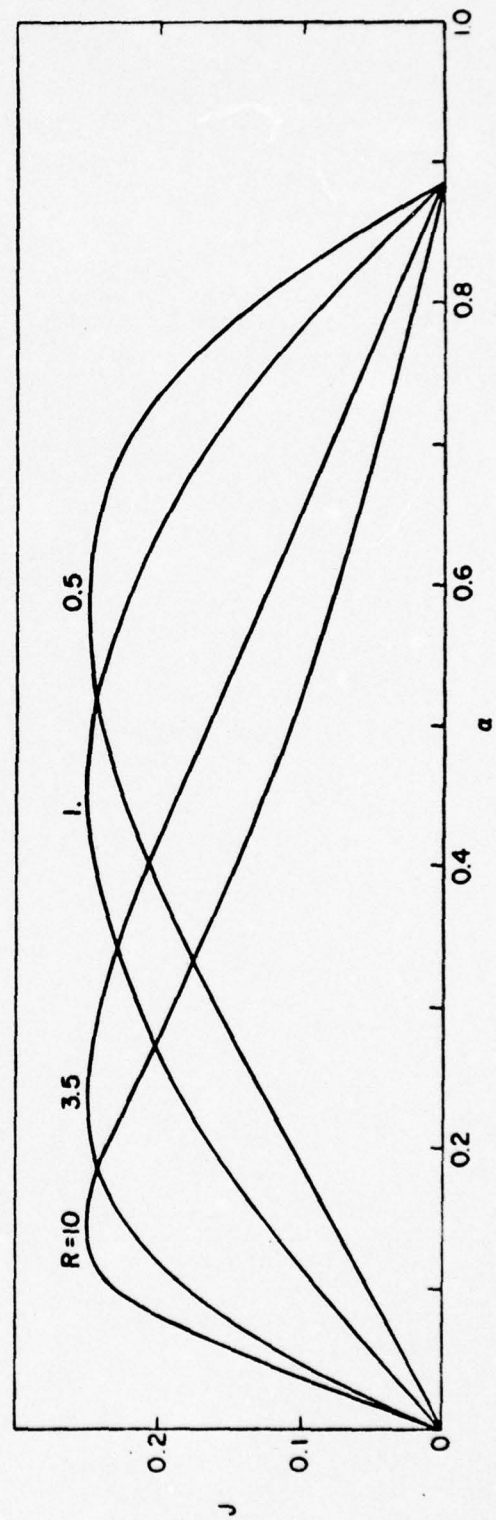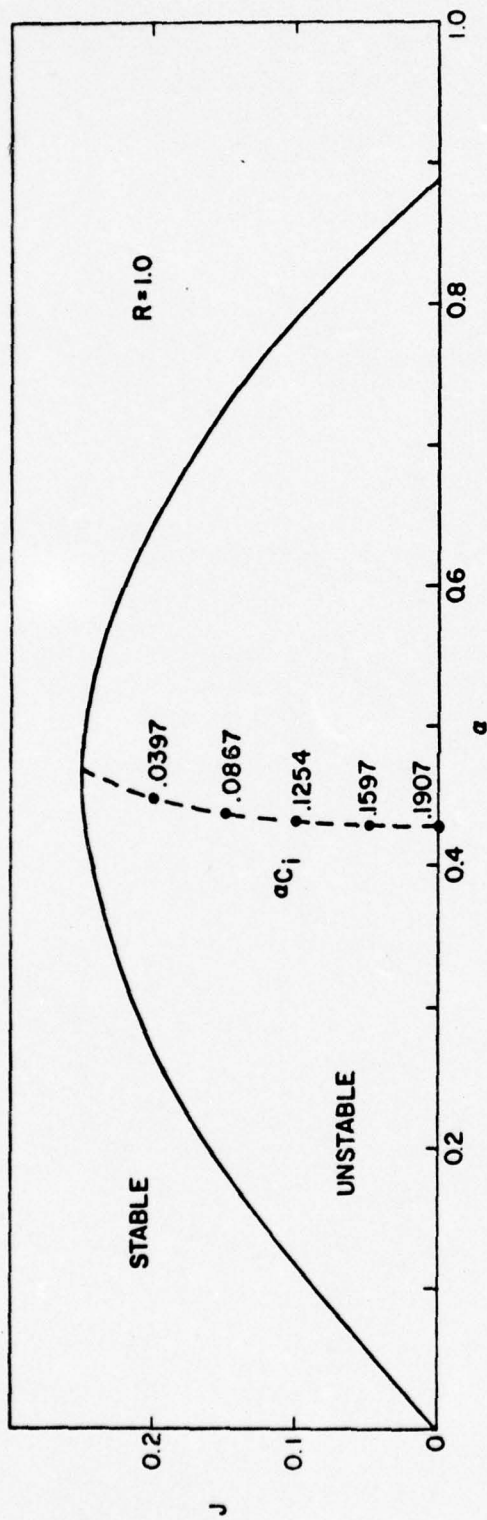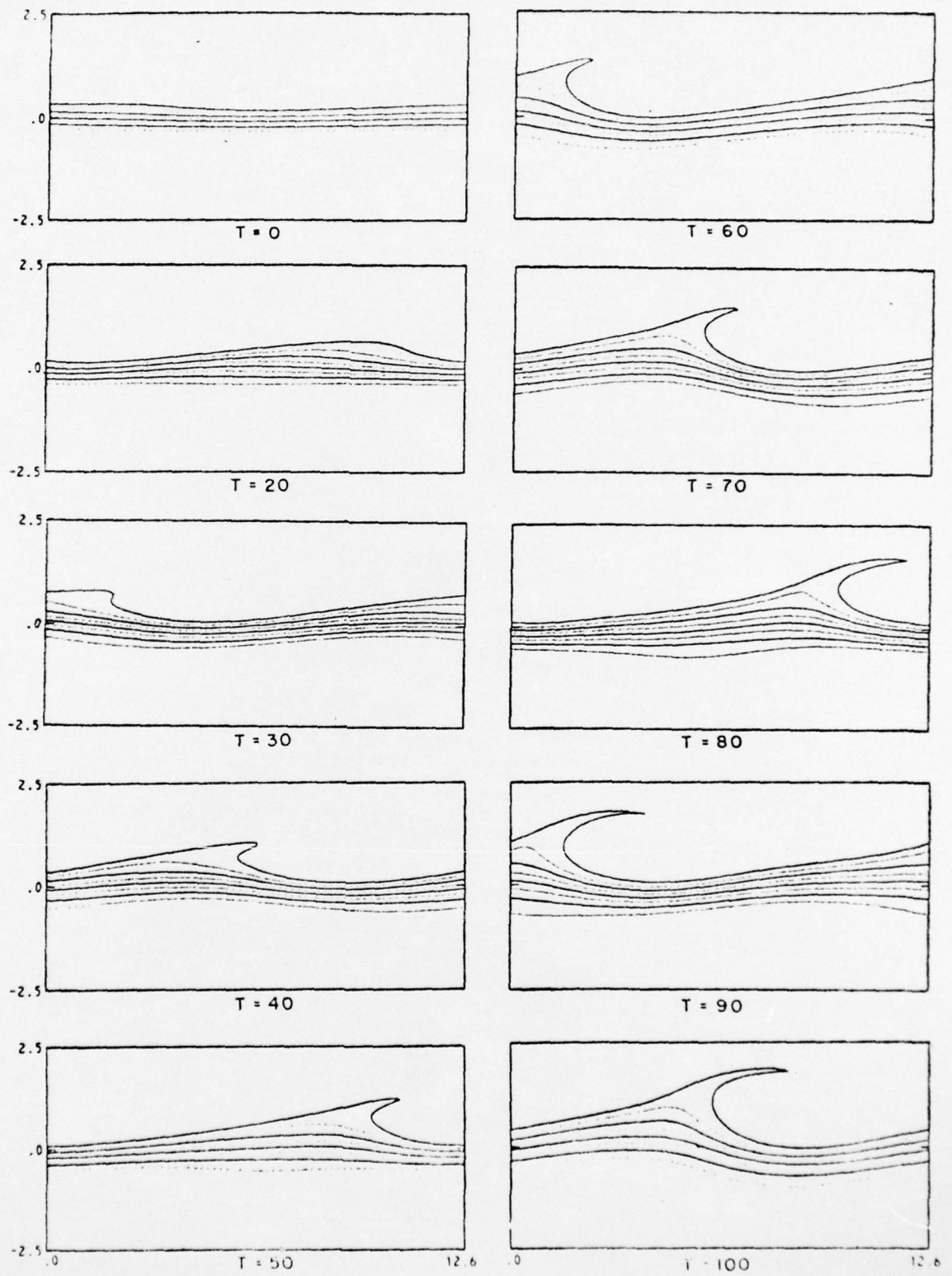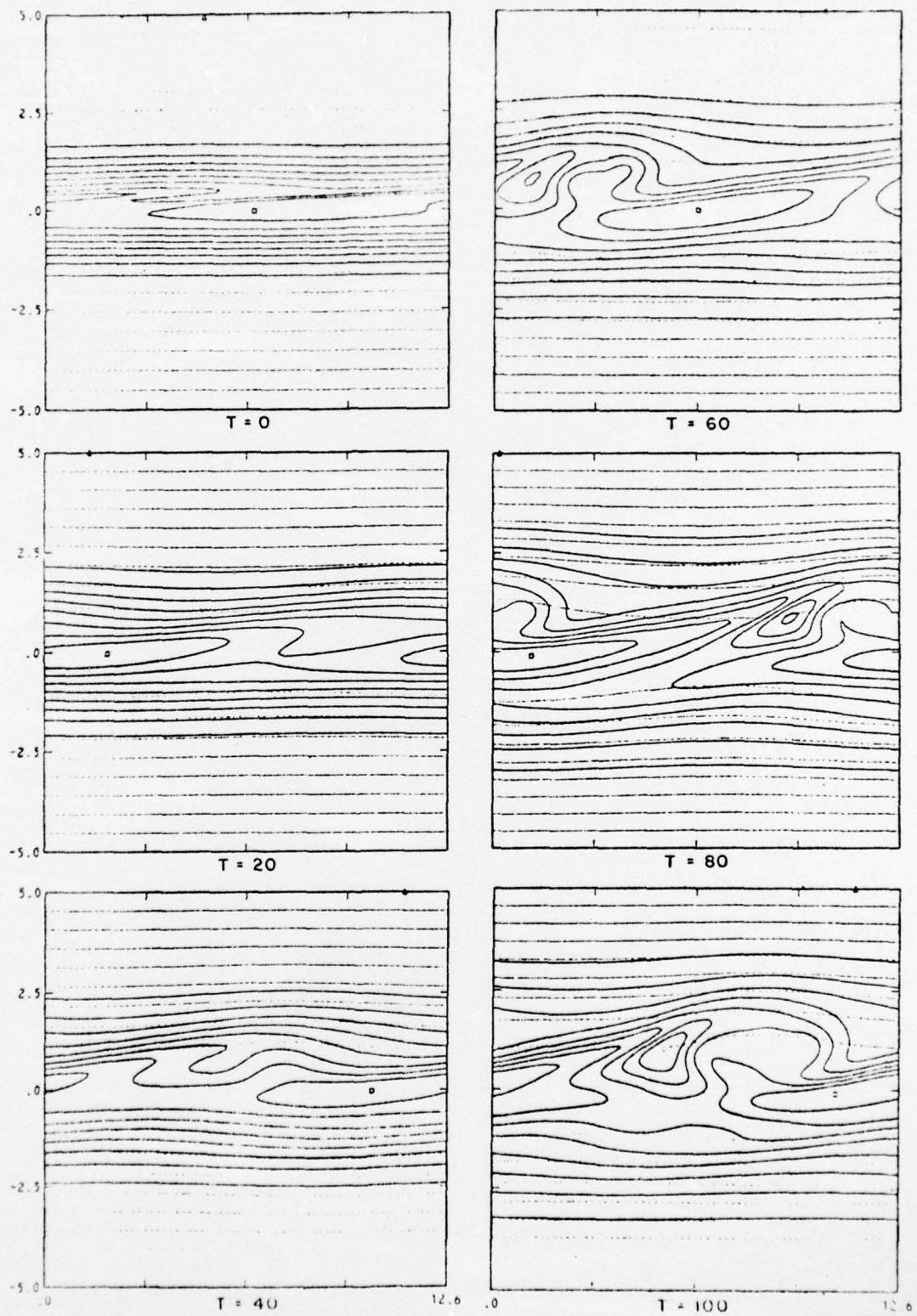
Figure 1
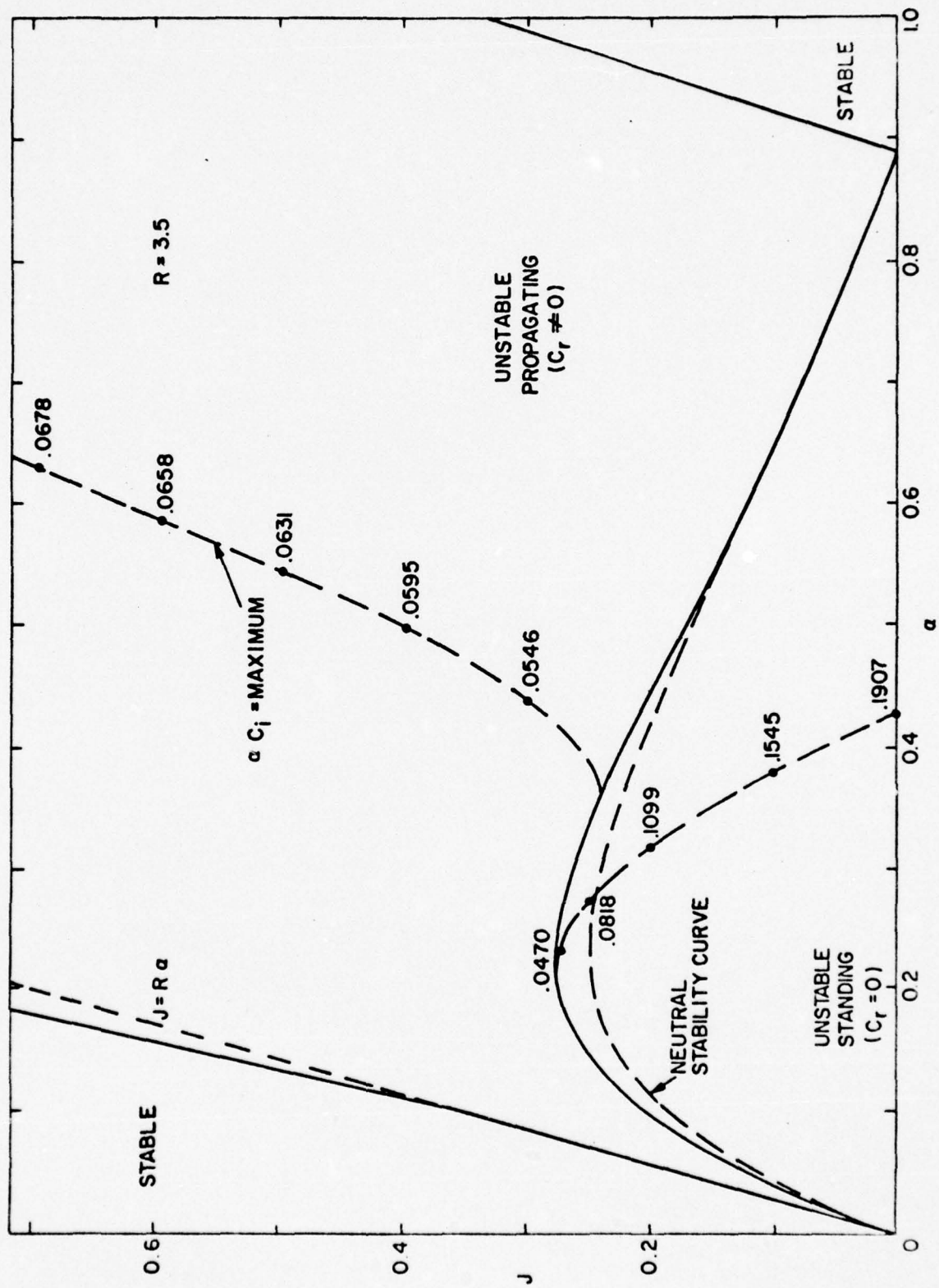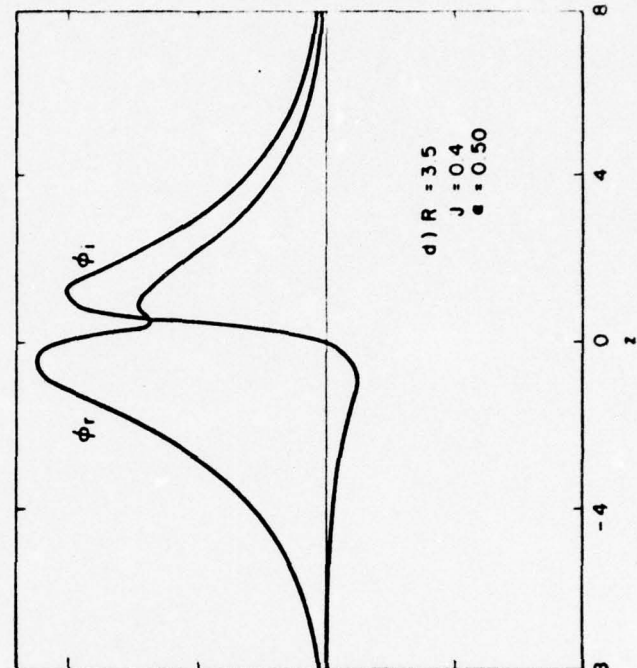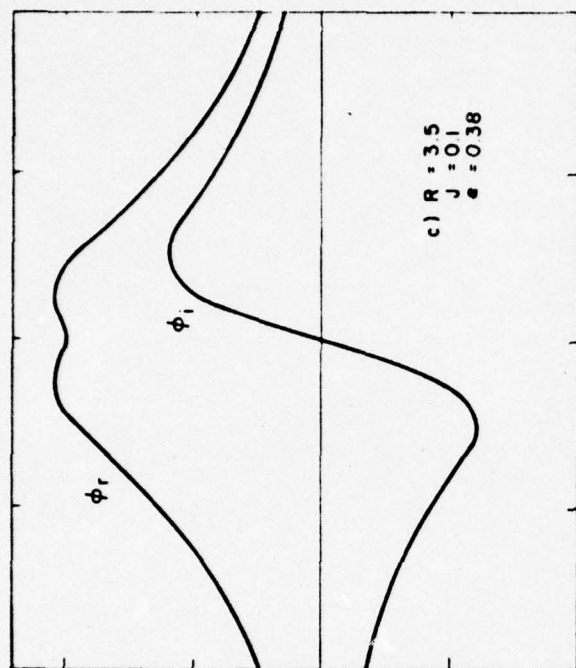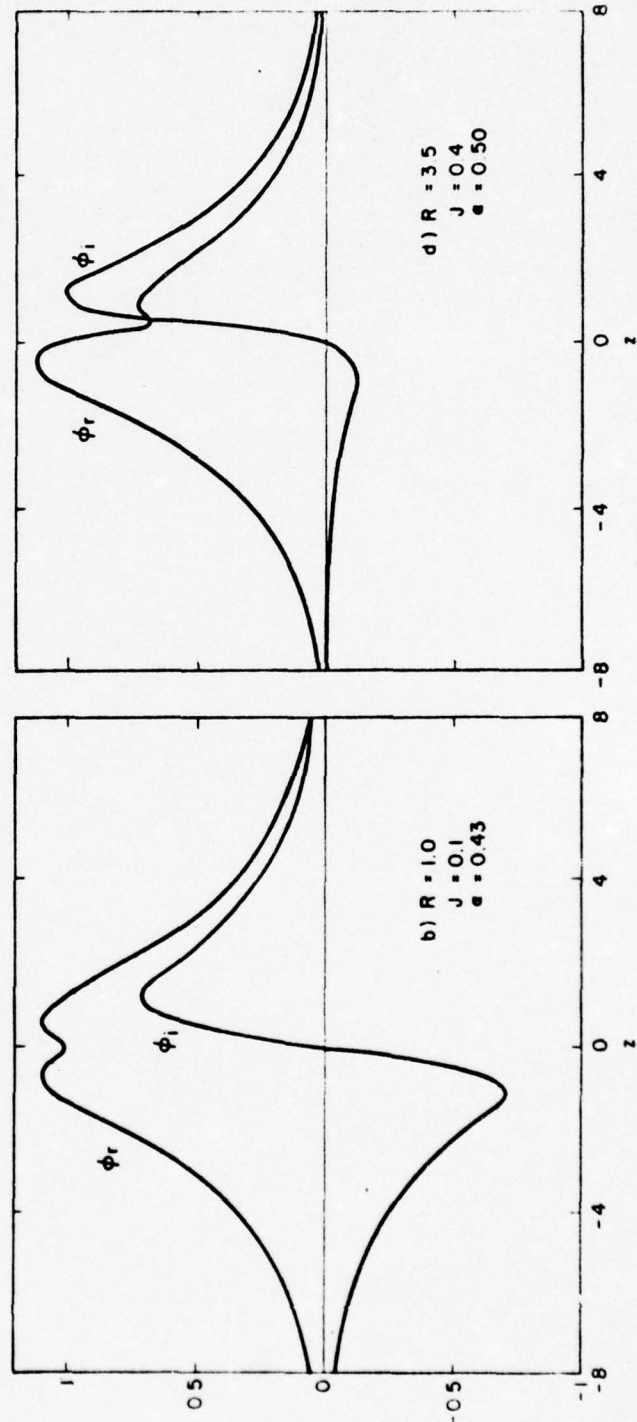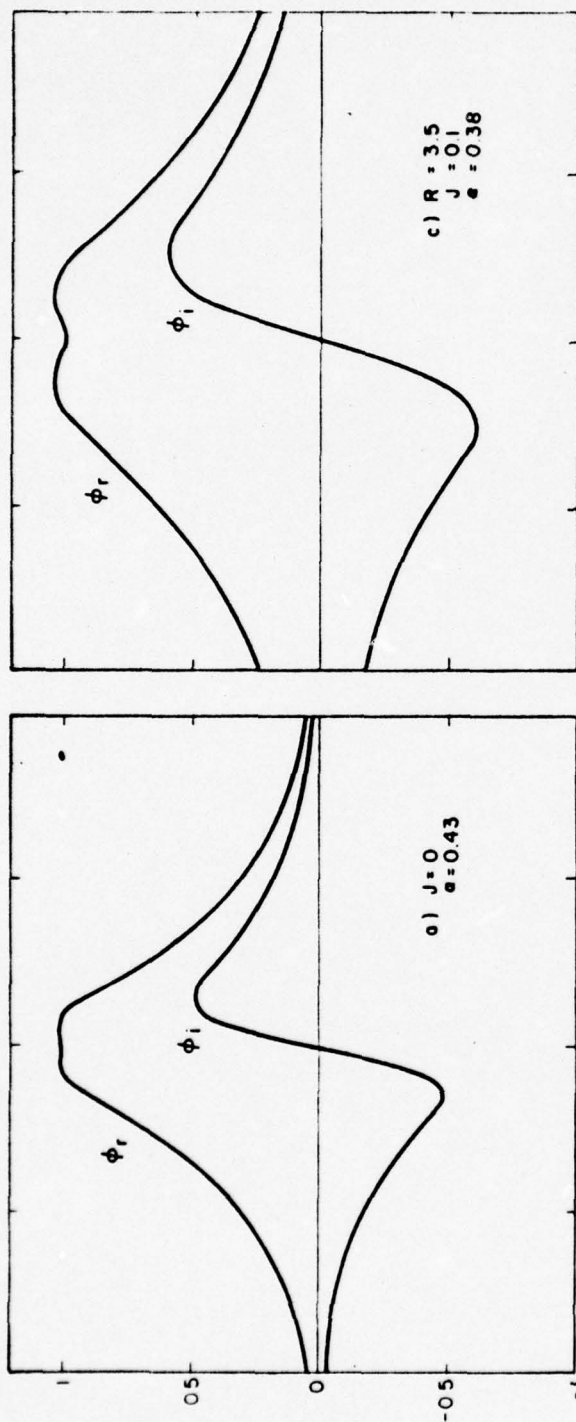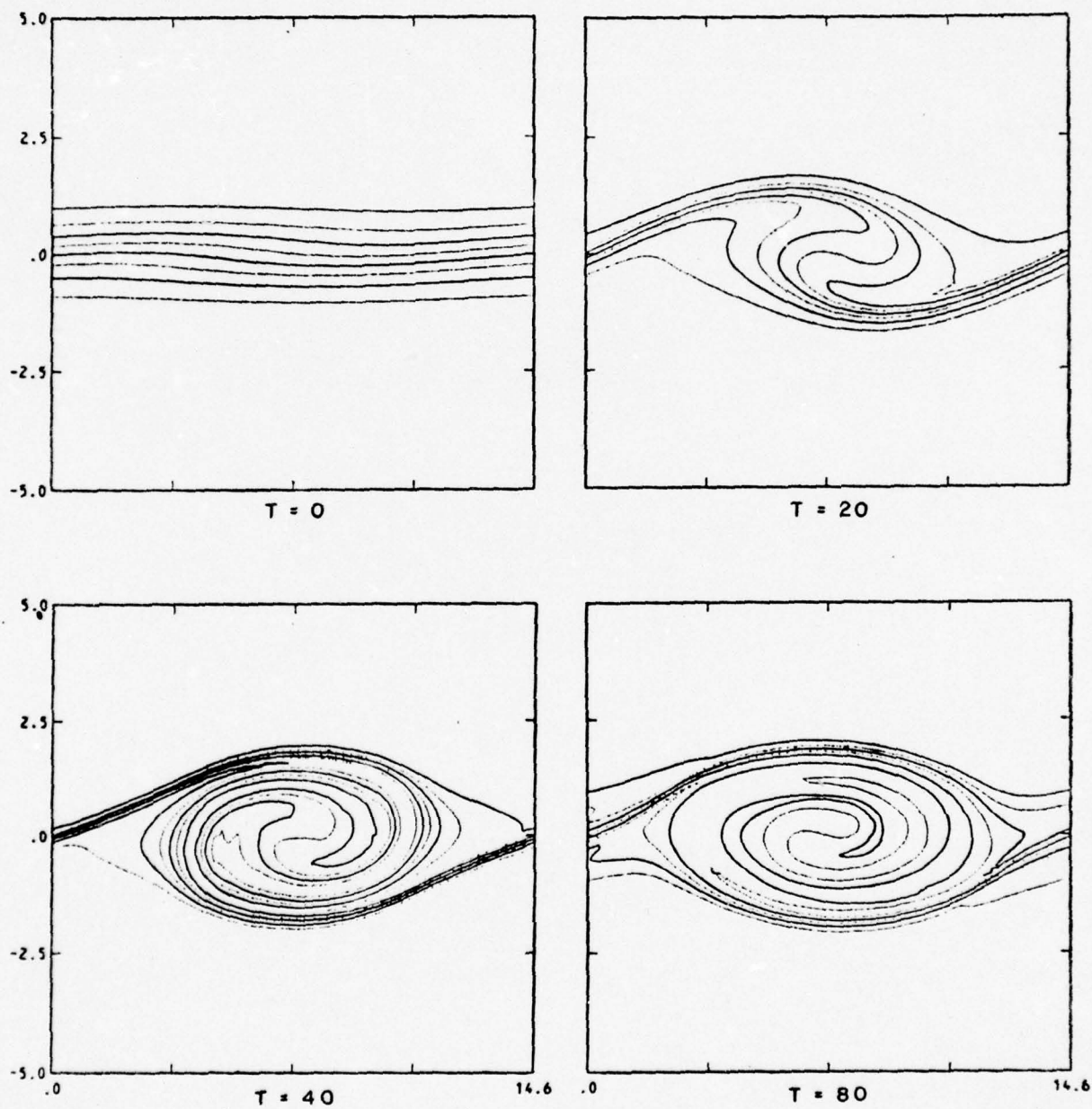
Figure 4
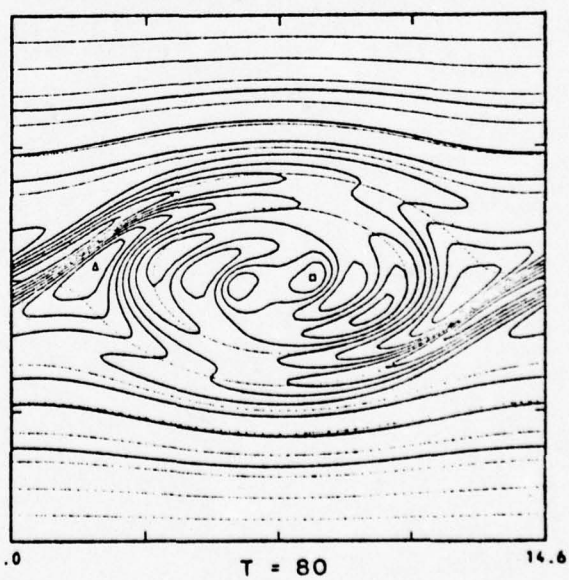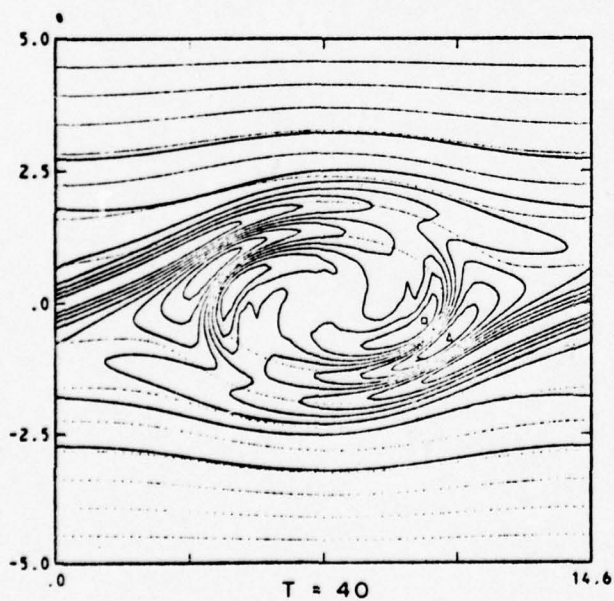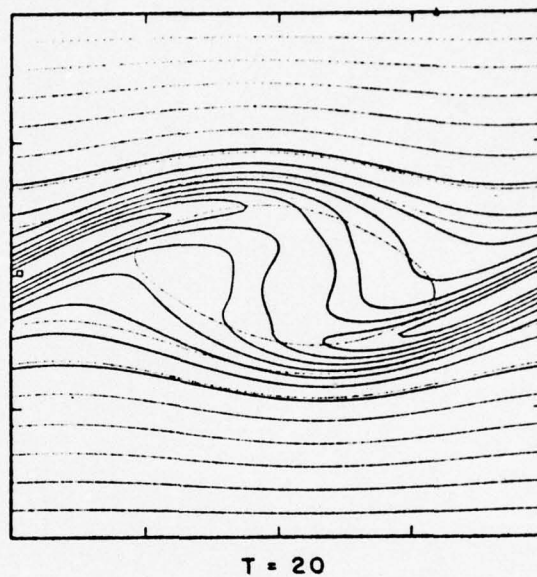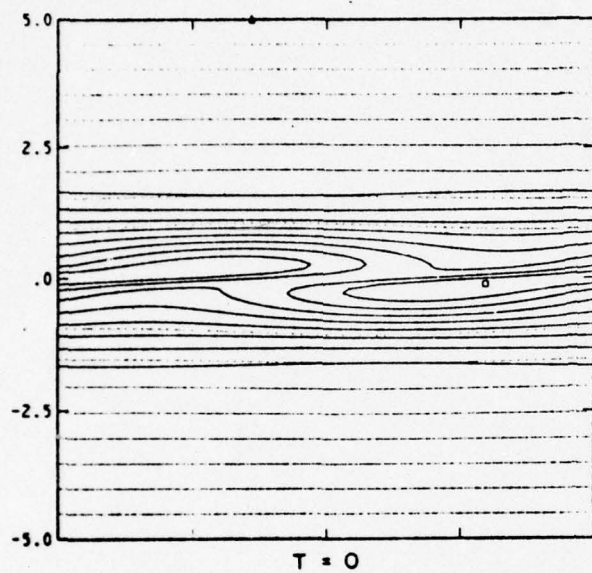
Figure 5
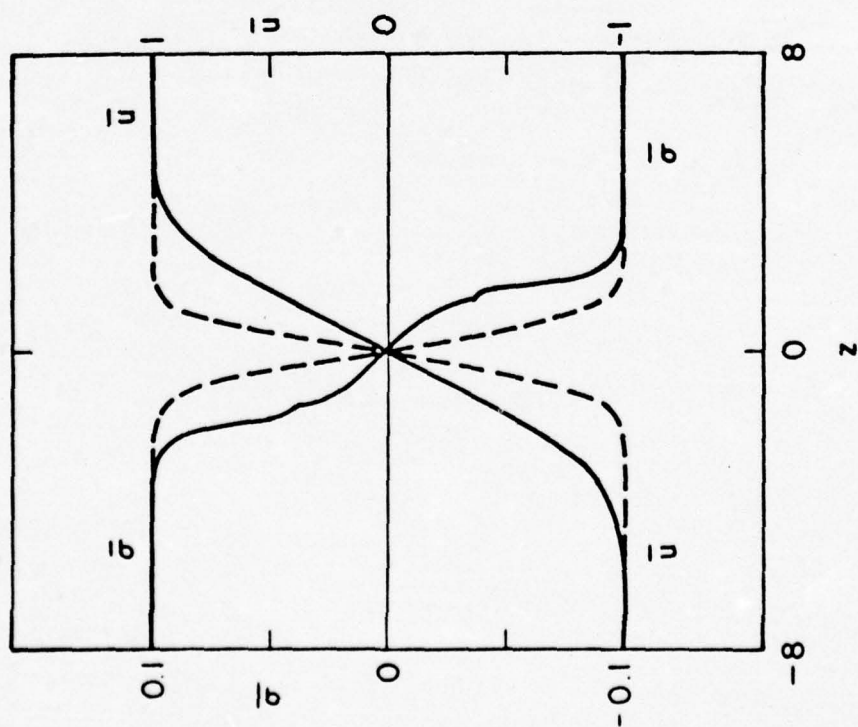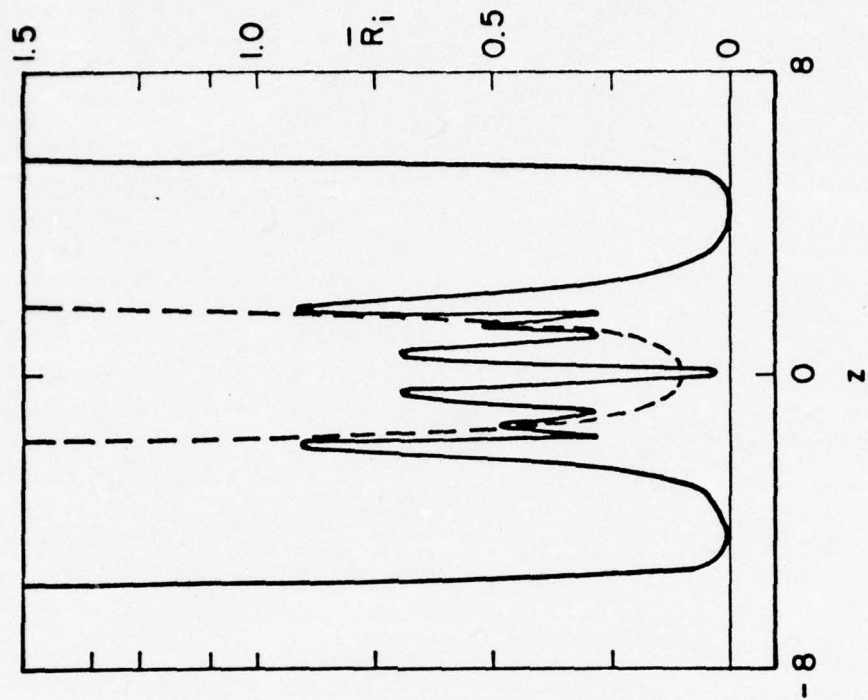
Figure 6
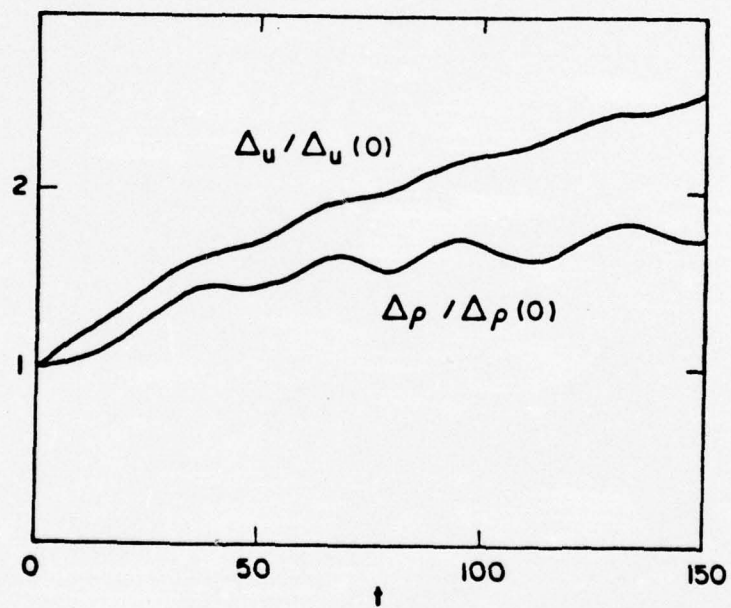
Figure 7

DISSIPATION, BUOYANCY FLUX AND REYNOLDS SHEAR STRESS (10^4)

FLUCTUATION ENERGY
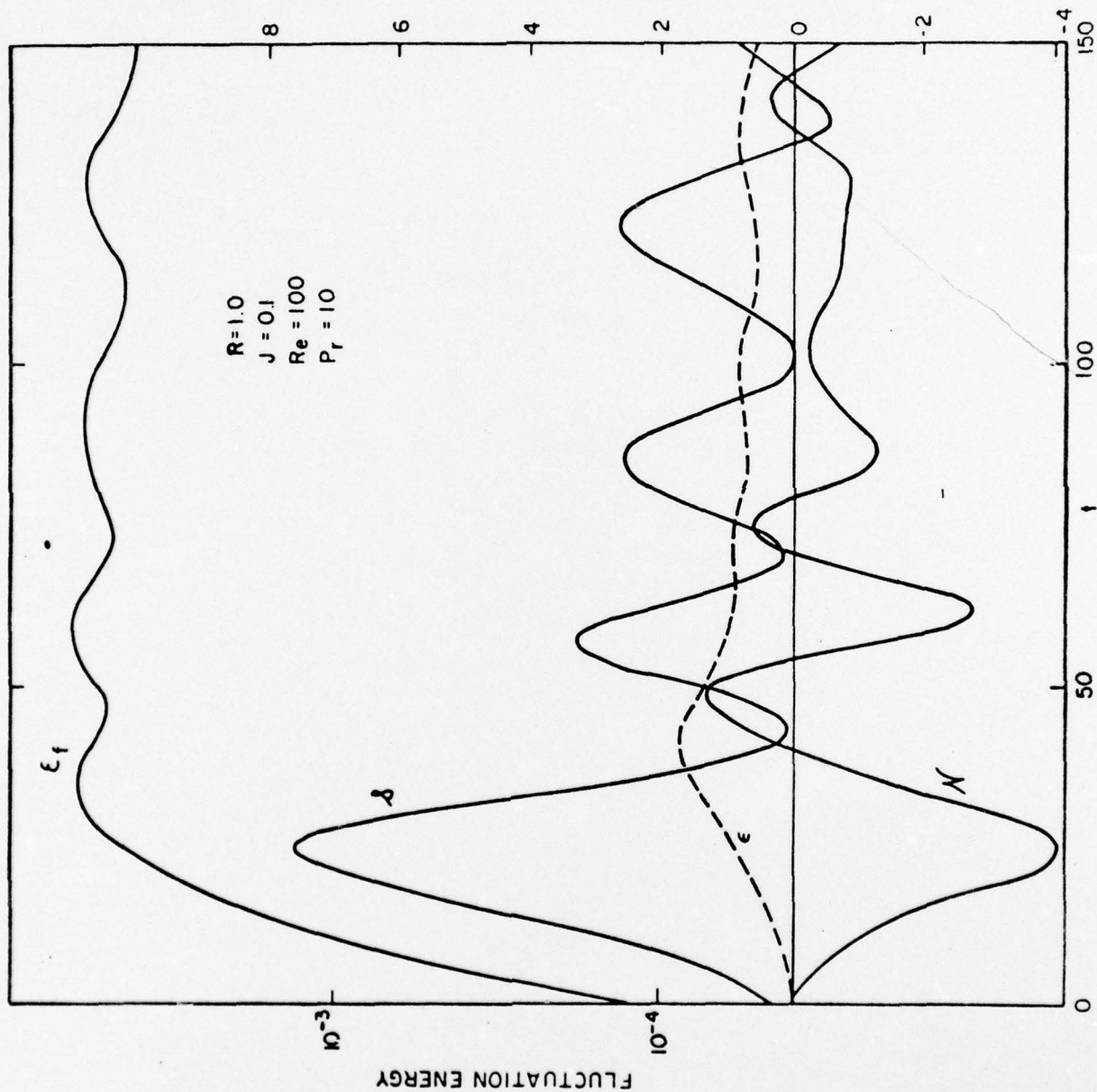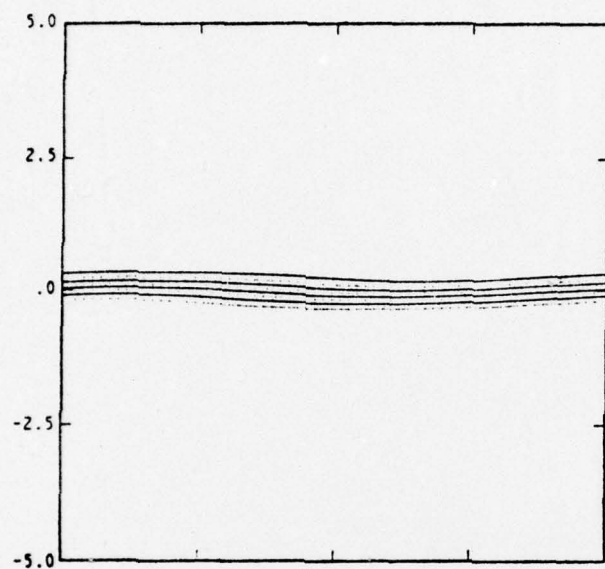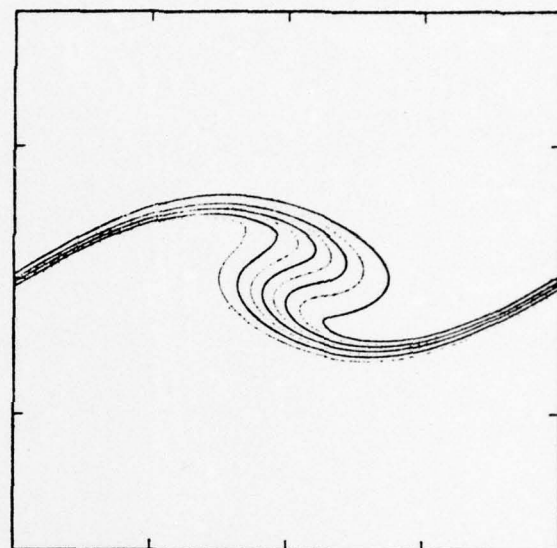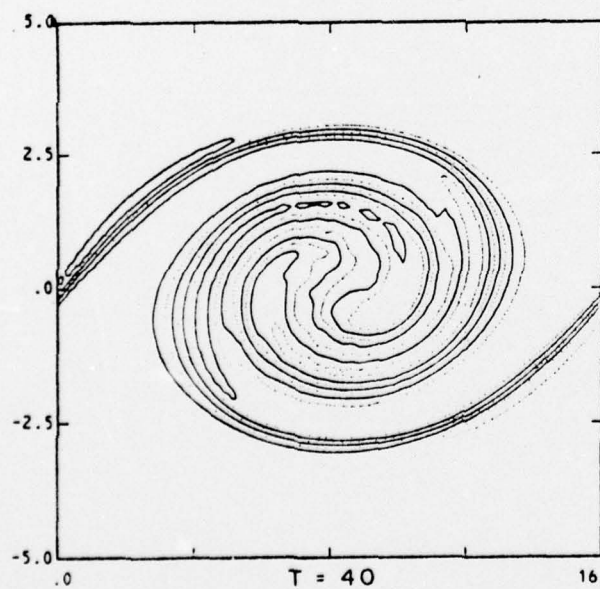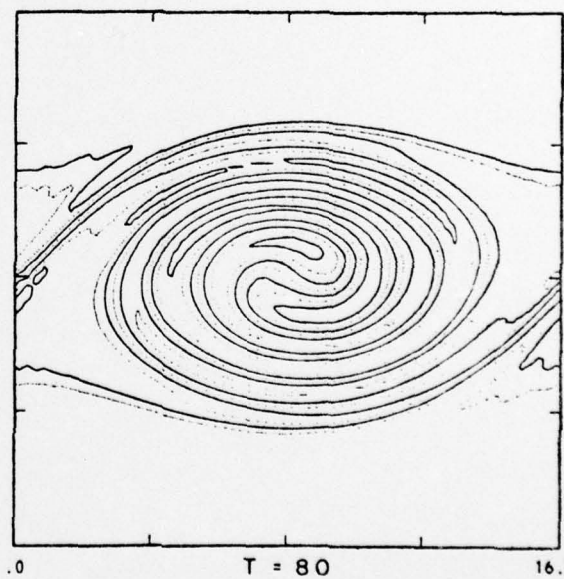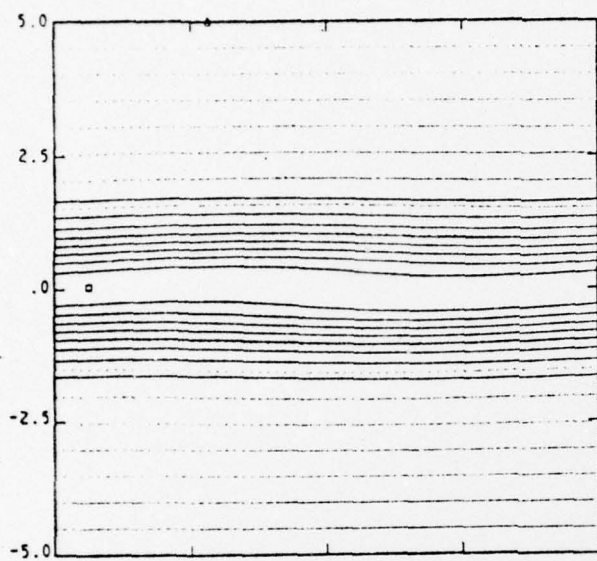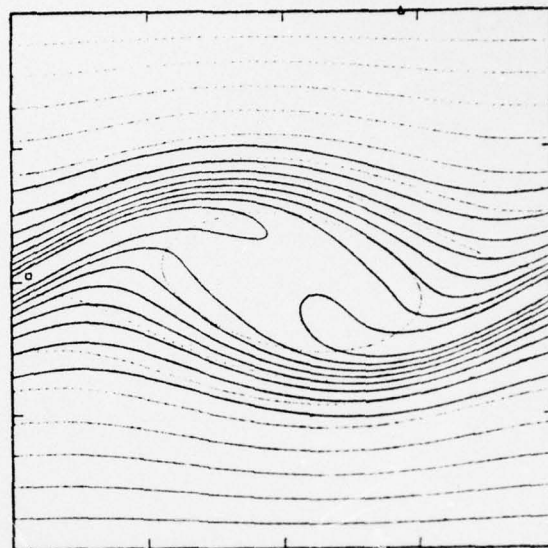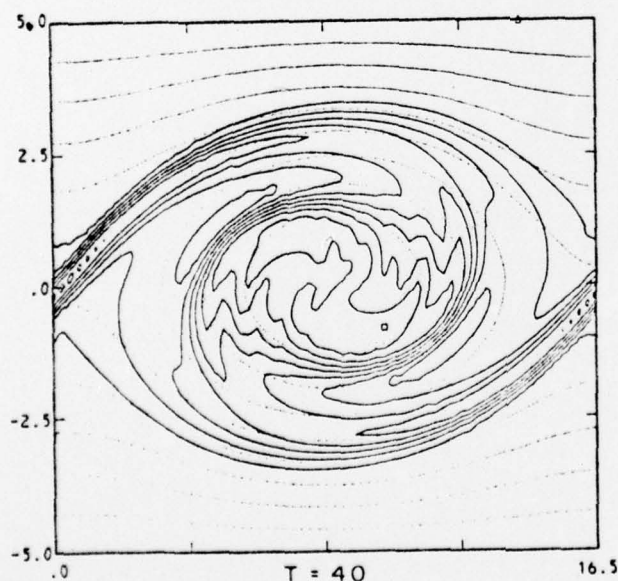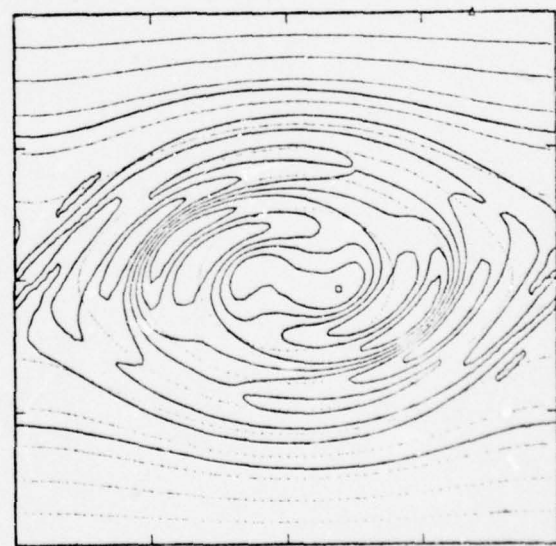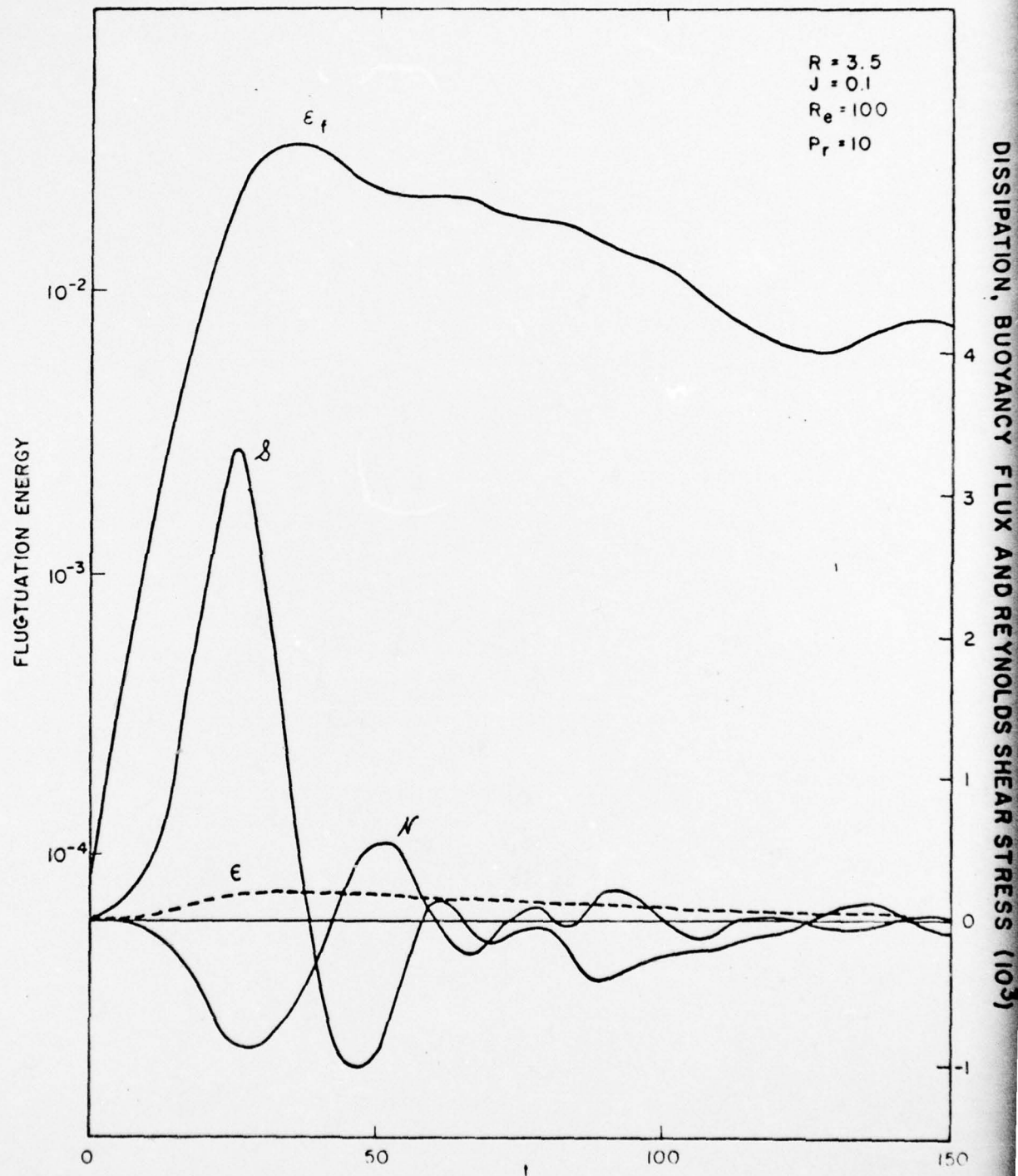
Figure 9

Figure 10

Figure 11

Figure 12

Figure 13

DENSITY

VORTICITY AND STREAM FUNCTION

T = 160

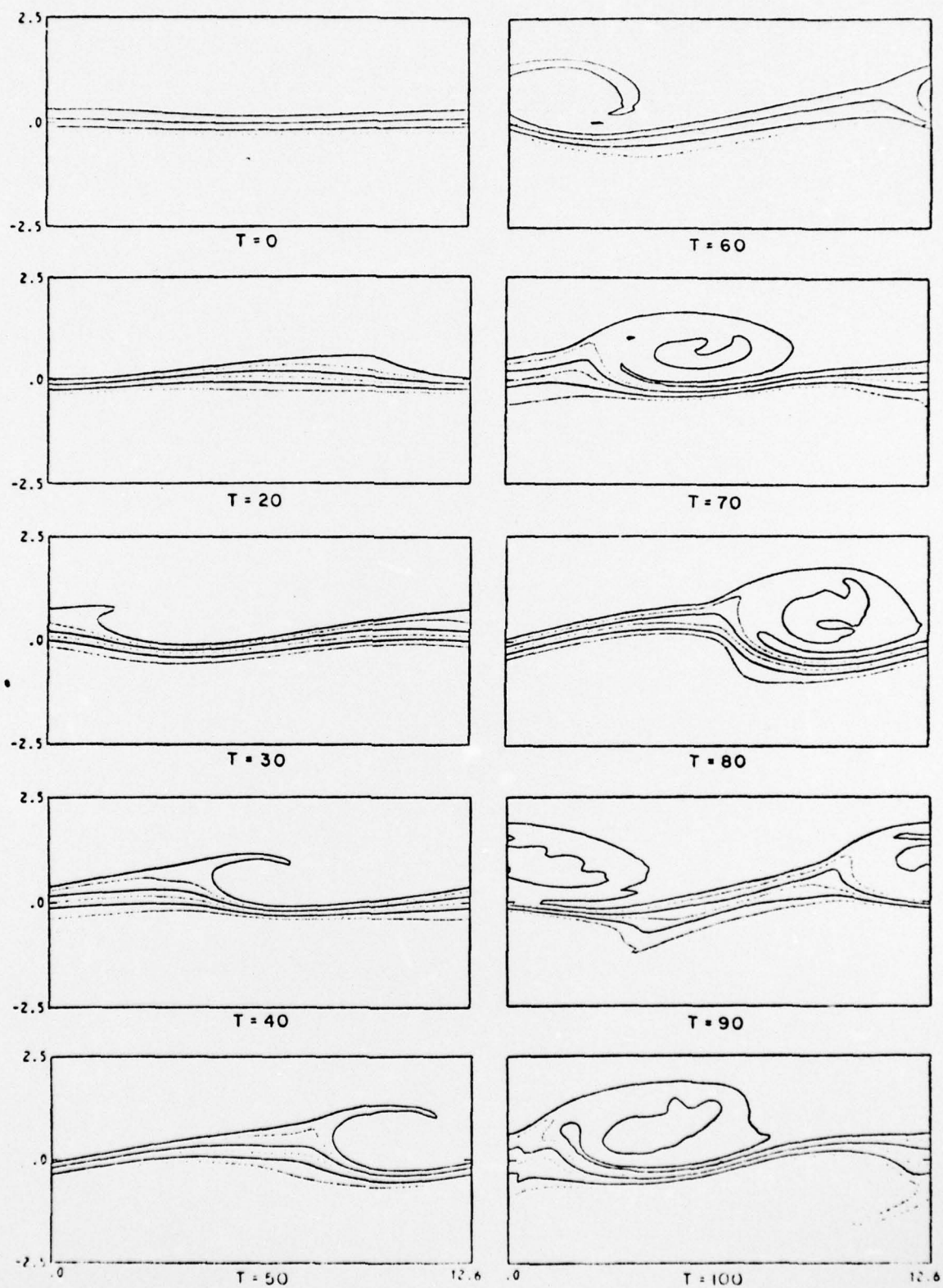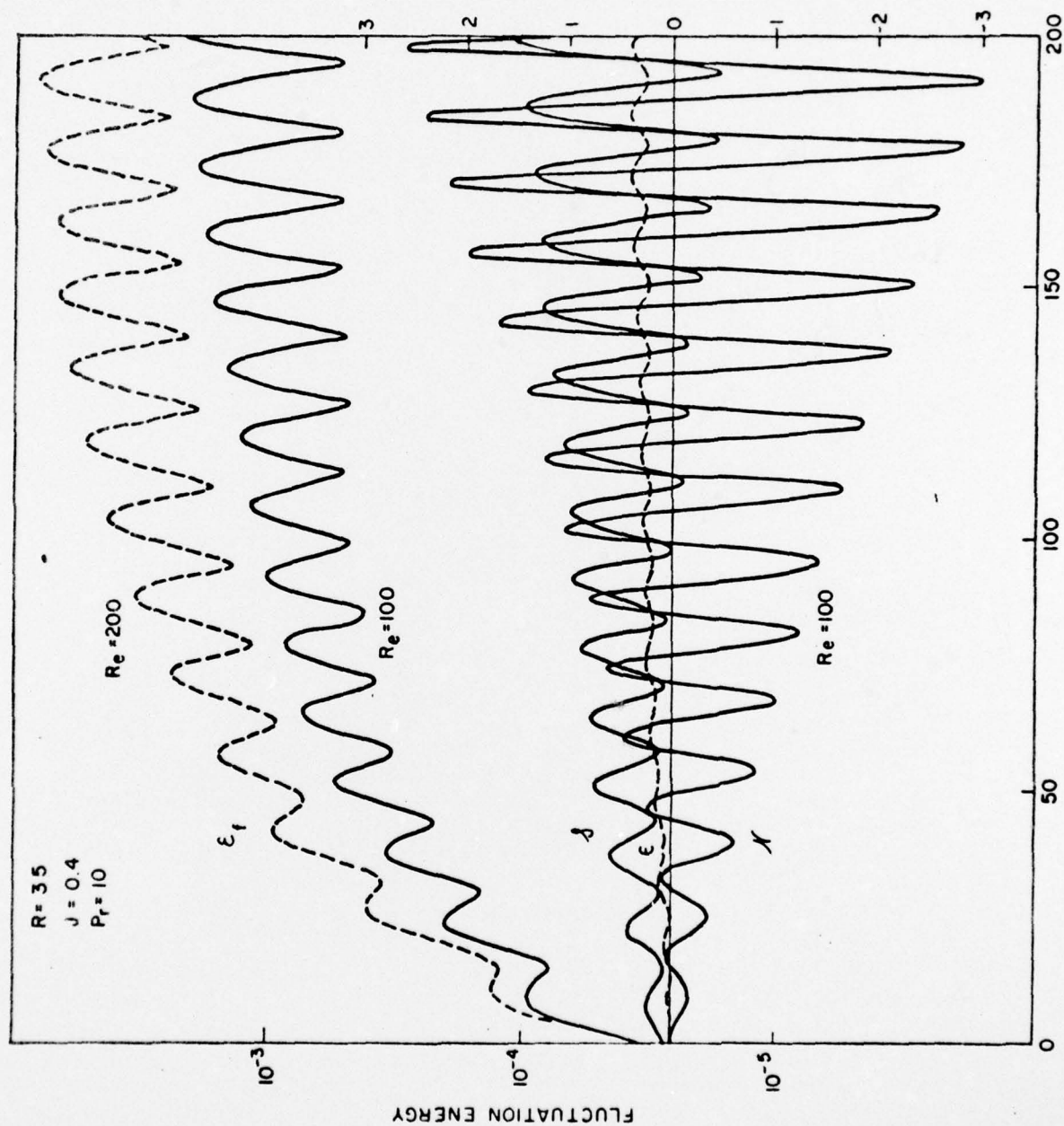T = 170

T = 180

T = 190

T = 200

T = 160

T = 180

T = 200
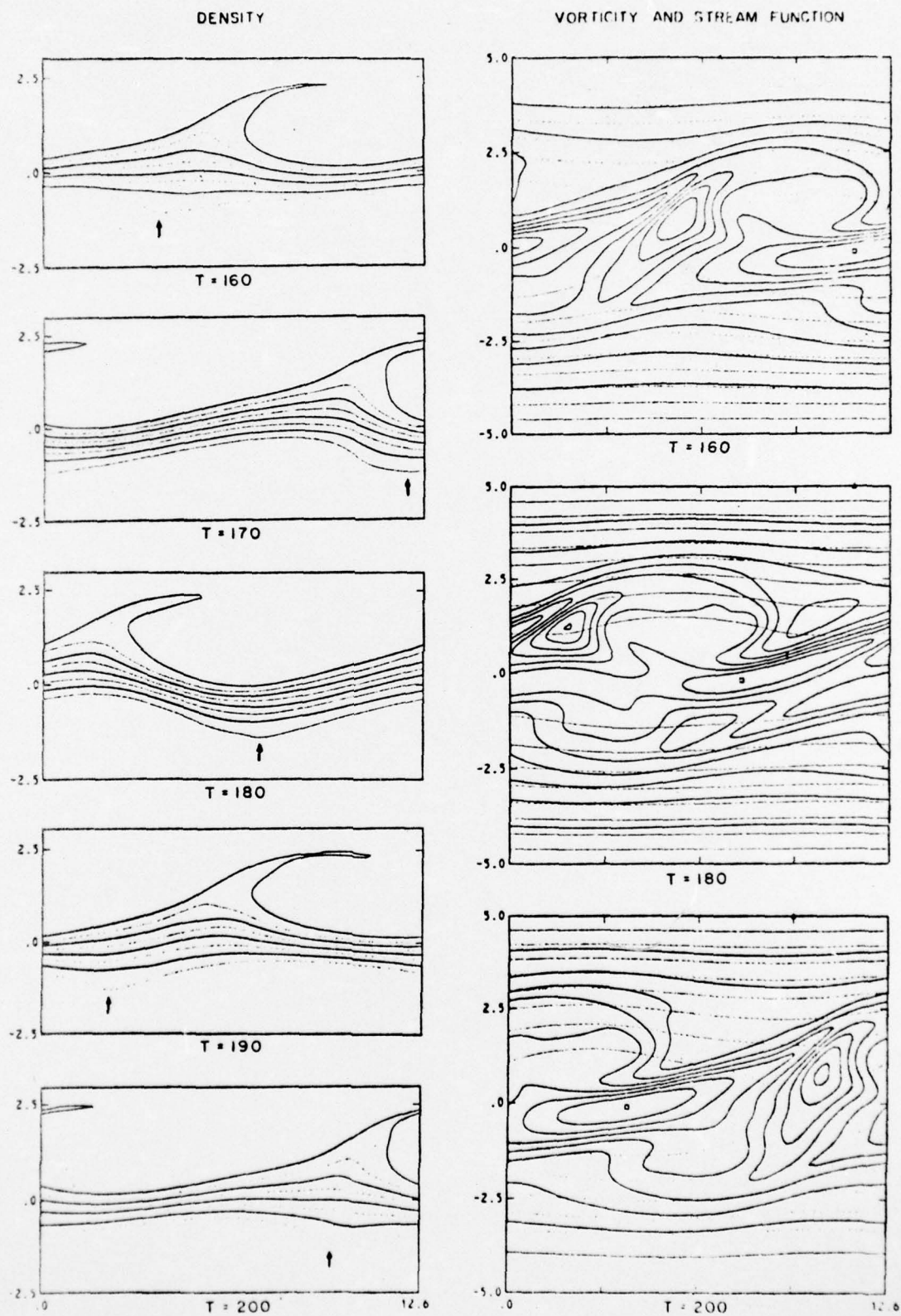
Figure 14

Figure 15

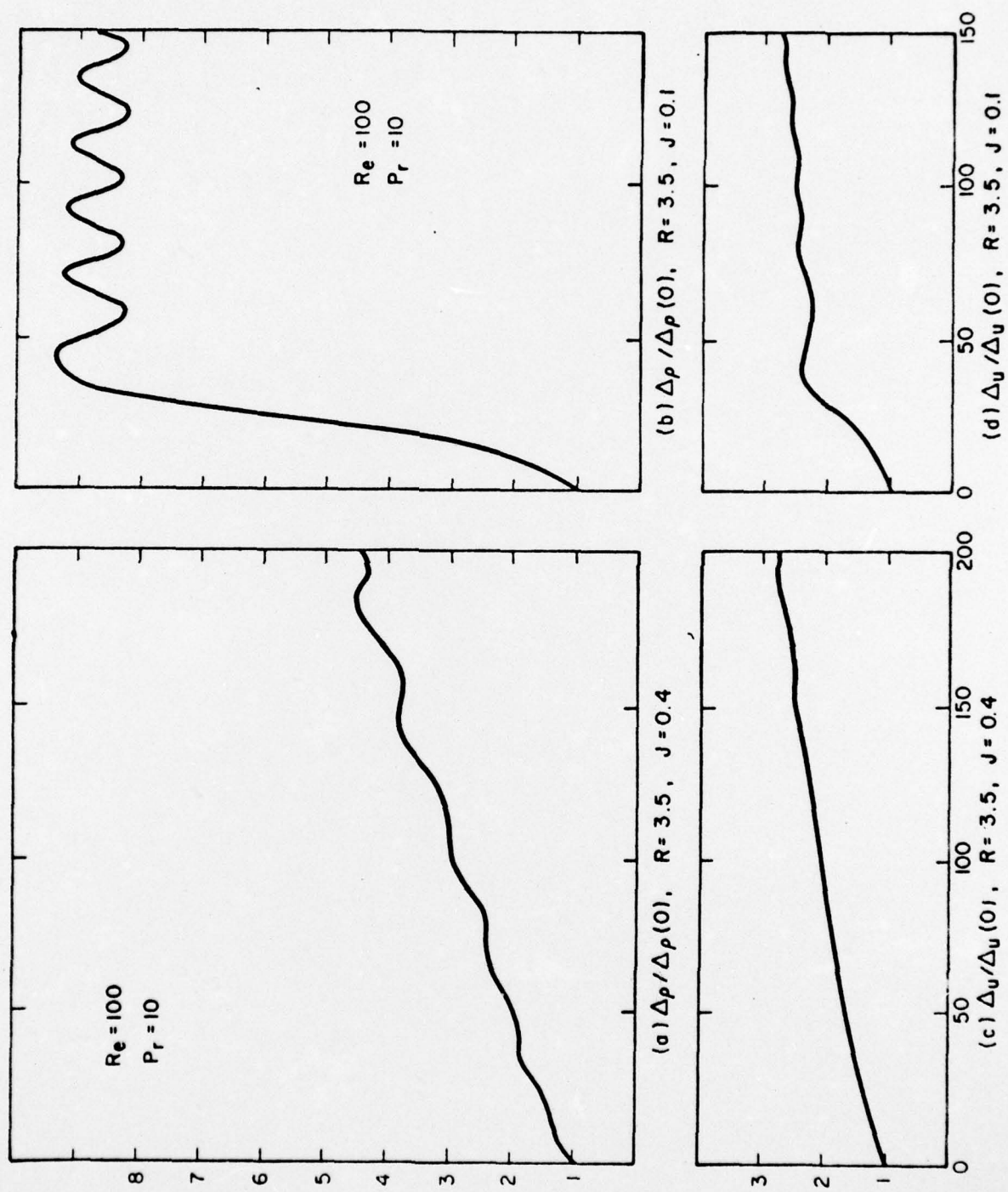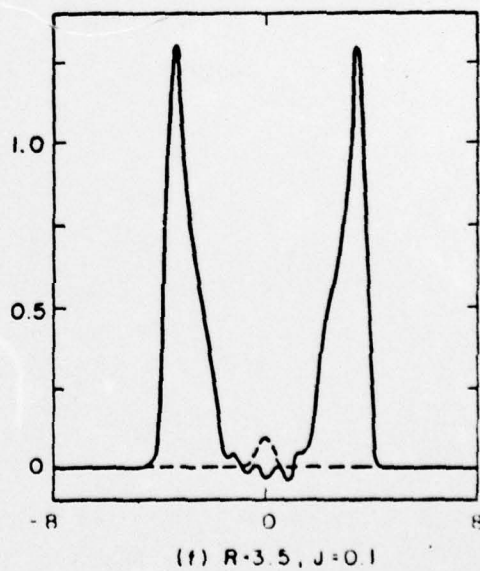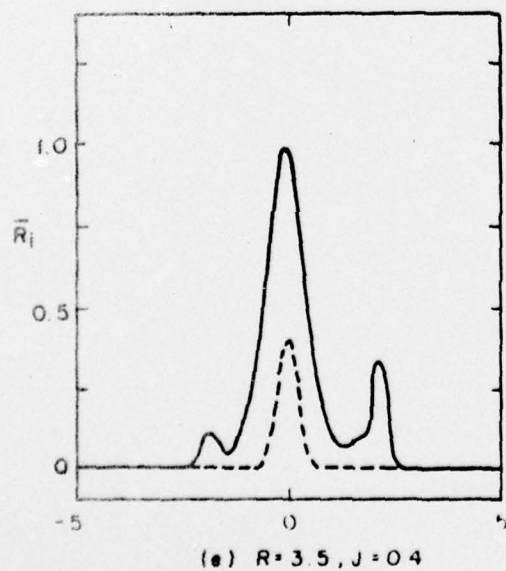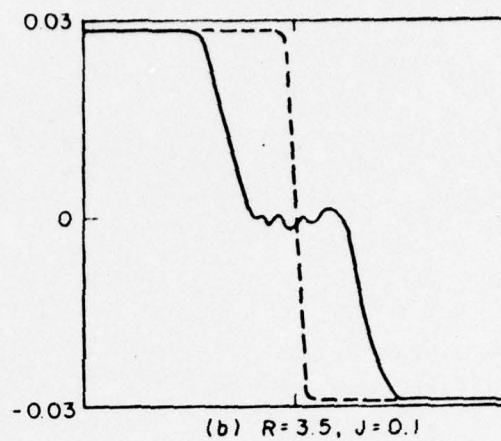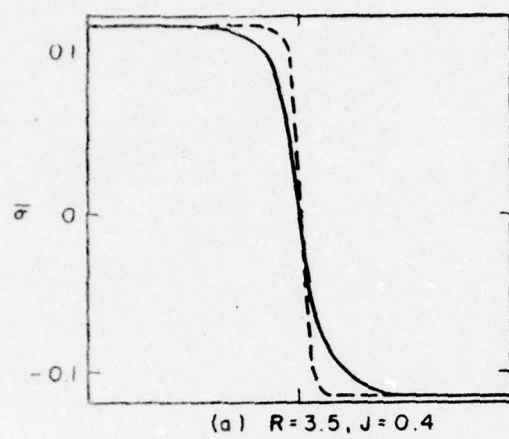DISSIPATION, BUOYANCY FLUX AND REYNOLDS SHEAR STRESS (X10^4)

Figure 16

$R_e = 100$
$P_r = 10$

$R_e = 100$
$P_r = 10$

(a) $\Delta_\rho / \Delta_\rho(0)$, $R = 3.5$, $J = 0.4$

(b) $\Delta_\rho / \Delta_\rho(0)$, $R = 3.5$, $J = 0.1$

(c) $\Delta_u / \Delta_u(0)$, $R = 3.5$, $J = 0.4$

(d) $\Delta_u / \Delta_u(0)$, $R = 3.5$, $J = 0.1$

Figure 17

(a) R = 3.5, J = 0.4

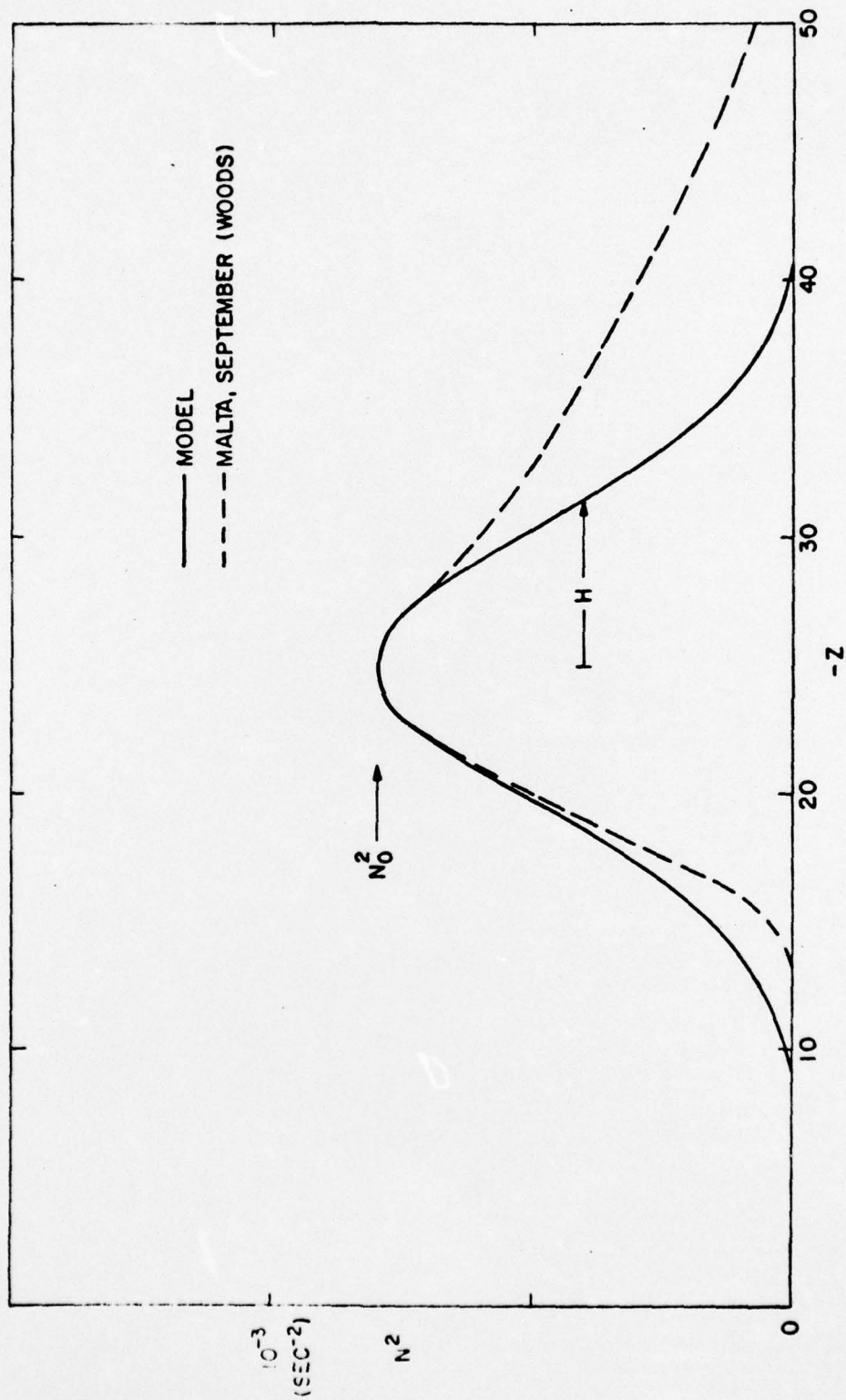(b) R = 3.5, J = 0.1

(c) R = 3.5, J = 0.4

(d) R = 3.5, J = 0.1

(e) R = 3.5, J = 0.4

(f) R = 3.5, J = 0.1
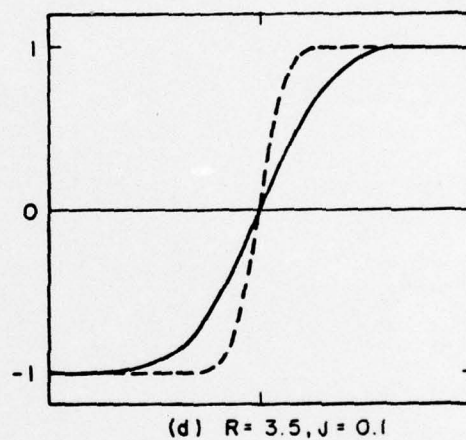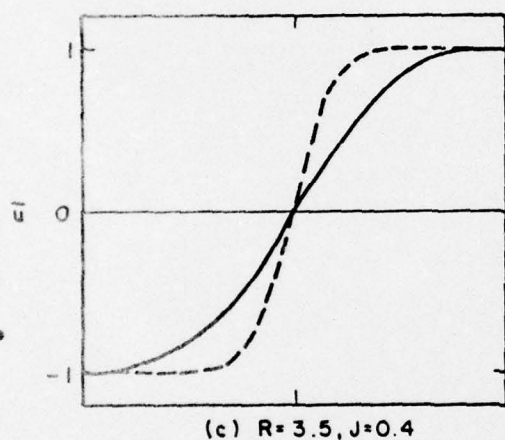
Figure 18

Figure 19

Figure 20

L/h

Figure 21